Available online at www.sciencedirect.com
ScienceDirect
Journal of Nuclear Materials 372 (2008) 182–214
journal of nuclear materials
www.elsevier.com/locate/jnucmat

In-reactor deformation of cold-worked Zr–2.5Nb pressure tubes

R.A. Holt *

Department of Mechanical and Materials Engineering, Queen's University at Kingston, Ont., Canada K7L 1W9

Received 20 March 2006; accepted 20 February 2007

Abstract

Over forty years of in-reactor testing and over thirty years of operating experience in power reactors have provided a broad understanding of the in-reactor deformation of cold-worked Zr–2.5Nb pressure tubes, and an extensive data-base upon which to base models for managing the life of existing reactors and for designing new ones. The effects of the major operating variables and many of the metallurgical variables are broadly understood. The deformation is often considered to comprise three components: thermal creep, irradiation growth and irradiation creep. Of the three, irradiation growth is best understood – it is thought to be driven by the diffusional anisotropy difference (DAD). It is still not clear whether the enhancement of creep by irradiation is due to climb-plus-glide (CPG), stress-induced preferred absorption (SIPA) or elasto-diffusion (ED). The least understood area is the transition between thermal creep and irradiation where the fast neutron flux may either suppress or enhance the creep rate. The three components are generally treated as additive in the models, although it is recognized that this is only a crude approximation of reality. There are still significant gaps in our knowledge besides the thermal- to irradiation-creep transition, for example, the effect of Mo which is produced from Nb by transmutation in the thermal neutron flux is not known, and on-going work is required in a number of areas. This paper reviews the current state of knowledge of the in-reactor deformation of cold-worked Zr–2.5Nb pressure tubes, and highlights areas for further research.

1. Introduction

The fuel channel of the CANDU®[1] nuclear power plant comprises a Zr–2.5Nb pressure tube and two steel end-fittings (in contact with the primary coolant), a Zircaloy-2 calandria tube (in contact with the moderator), and four spacers maintaining the annular gap between pressure tube and calandria tube. The pressure tubes are the primary containment of the high temperature D_2O inside the core of a CANDU® reactor. They are subjected to high stresses, temperatures and fast neutron fluxes which cause changes in the dimensions and material properties. In addition, service-induced wear occurs. To ensure the safe, reliable and economic performance of the reactor, it is important that these changes are known and that the rate of change can be predicted and demonstrated to remain within the design basis. The pressure tubes are designed, specified, manufactured and operated to standards published by the Canadian Standards Association [1–6].

1.1. Fuel channel design

The core of a CANDU® reactor is a cylindrical tank (calandria) containing D_2O moderator at 70 °C. It is penetrated by 380 (675 MW units) or 480 (875 MW units) horizontal fuel channels, Fig. 1.1.1. The cold-worked Zr–2.5 wt% Nb pressure tube is 6 m long, 104 mm in diameter and has a wall thickness of 4.2 mm. The chemical specification for the alloy is given in Table 1.1. The pressure tube contains the natural UO_2 fuel, encased in Zircaloy-4 sheathing, and heat transport fluid, D_2O, operating at temperatures from 520 to 540 K at the inlet to 565–585 K at the outlet. The inlet pressure is about 10.5 MPa and the outlet pressure is about 9.9 MPa, resulting in an initial axial stress in the pressure tube wall of about 65 MPa and an initial hoop stress that varies from about 130 MPa at the inlet to about 122 MPa at the outlet. Superposed on the axial stress from

* Fax: +1 613 533 6610.
E-mail address: holt@me.queensu.ca
[1] CANDU® is the registered trademark of AECL.

0022-3115/$ - see front matter © 2007 Elsevier B.V. All rights reserved.
doi:10.1016/j.jnucmat.2007.02.017

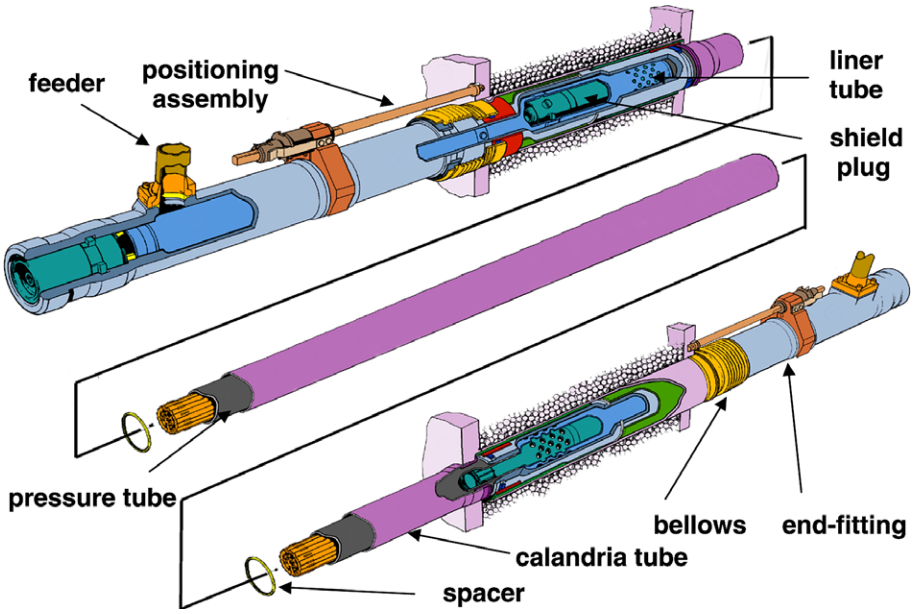

Fig. 1.1.1. Schematic diagram of a CANDU fuel channel.

Table 1.1
Chemical specification for Zr–2.5Nb pressure tubes for CANDU reactors

Element	Limits (by weight)
Niobium	2.4–2.8%
Oxygen	900–1300 ppm
Nitrogen	<65 ppm
Hydrogen	Was <20 ppm, now <5 ppm
Iron	<1300 ppm

the pressure is a relatively small axial component due to an end-load from the out of core hardware that varies with time from tensile to compressive. The peak fast flux is up to 3.5×10^{17} n m^{-2} s^{-1}, $E > 1$ MeV. The pressure tube and the annealed Zircaloy-2 calandria tube are separated by spacers and the annular gap is filled with flowing CO_2 to insulate the pressure tube from the cold moderator. The calandria tube has a wall thickness of 1.4 mm and an inside diameter of 129 mm. The pressure tubes are rolled into 403 stainless steel end-fittings at each end of the channel. The end-fittings have mechanical closures to enable on-power refueling and are connected to the heat transport system (HTS) by carbon steel 'feeders'.

The annulus gas system has been developed to detect the presence of moisture if a leak develops in the primary pressure boundary inside the reactor core. The ability to detect moisture at an early stage of the formation of a sub-critical, through-wall crack in the pressure tube is an important component in assuring leak-before-break of the tubes.

1.2. Aging mechanisms

Pressure tubes must accommodate the following aging mechanisms [7–9]: dimensional changes, material property changes, deuterium ingress due to corrosion and in-service damage and wear. In older CANDU® units these changes were not fully understood, and have required monitoring, and in some cases maintenance. In newer CANDU stations adequate allowances for them have been made for the design life of the reactor.

To assess their aging characteristics, pressure tubes are subject to periodic non-destructive inspection, and material surveillance, which, in Canada, requires a pressure tube to be removed every three years from the unit with the highest integrated neutron fluence (lead unit), for evaluation of fracture properties. These requirements are defined in Ref. [5]. The data that has been obtained from the periodic inspection and surveillance programs has been supplemented by in-service inspection programs, destructive examination of tubes removed as a result of in-service damage and irradiation of small specimens in test reactors [10–13].

2. Deformation of pressure tubes

During reactor operation, the effects of temperature, stress and neutron flux change the dimensions of the pressure tubes. Irradiation and thermally induced deformation of fuel channel components will, in the absence of other mechanisms, eventually determine fuel channel life. The dimensional changes in pressure tubes during normal reactor operation are axial elongation, diametral expansion, sag and wall thinning. One can consider that there are three mechanisms contributing to the dimensional changes: irradiation growth – the change in shape at constant volume in a fast neutron flux, thermal creep – the change in shape due to the effect of temperature and stress in the absence of a fast neutron flux, and irradiation creep, the additional change in shape due to stress and fast neutron flux [14].

To a first approximation the total in-reactor deformation rate is often expressed as the sum of these three terms, i.e.,

$$\dot{\varepsilon}_{\mathrm{d}}^{\mathrm{total}} = \dot{\varepsilon}_{\mathrm{d}}^{\mathrm{g}} + \dot{\varepsilon}_{\mathrm{d}}^{\mathrm{ic}} + \dot{\varepsilon}_{\mathrm{d}}^{\mathrm{tc}}, \tag{2.1}$$

where $\dot{\varepsilon}$ is strain rate and the subscript d indicates the direction, and superscripts, g, ic and tc designate growth, irradiation creep and in-reactor thermal creep, respectively.

To some extent, the creep and growth phenomena can be studied independently to determine their important characteristics, however the real behaviour is more complex than this, representing a continuum in a multi-dimensional space of stress, fast neutron flux, temperature, fast neutron fluence and the microstructure of the material.

The changes in dimensions cause the stress state in the pressure tube to vary with time, for example, while the coolant pressure profile along the channel remains essentially constant with time, the internal diameter increases, and the wall thickness is reduced, resulting in an increase in the hoop stress. The change in the stress state must be taken into account to understand and predict the behaviour accurately.

The main trends of pressure tube deformation at normal operating conditions were fairly well established by the early 1980s based on various types of in-reactor testing in the NRU Reactor at Chalk River and early diametral and sag gauging results and elongation measurements from Pickering A [15]. In the past 20 years the emphasis has been on:

- extrapolating these results to newer reactors that operate at higher temperatures and with higher fast neutron fluxes [16];
- making end-of-life predictions requiring long term irradiations [12,17];
- understanding sag of the pressure tube and the development of contact between pressure tubes and calandria tubes [18–20];
- assessing the microstructural and microchemical changes that occur during service [21];

and most recently:

- identifying the causes of variability between reactors and between tubes in one reactor [22];
- creep at high stresses under multi-axial stress conditions near flaws [23,24];
- the transition between thermal- and radiation-induced creep near the ends of the tubes [25].

For general reading on in-reactor deformation of zirconium alloys, see Refs. [26,27].

2.1. Diametral expansion

Diametral expansion, which corresponds to an increase in the circumference of the tube, occurs mainly by irradiation creep [14]. There is a small thermal creep component and the contribution of irradiation growth component is actually negative, and therefore beneficial. The diametral strain is measured as mandated in Ref. [5]. For CANDU 6 reactors, approximately 90 diameter profiles have been measured up to 123 000 full power hours of operation, allowing statistical treatment of the data (examples of such data are given in Ref. [14]). A typical profile is shown in Fig. 2.1.1, and typical fast neutron flux and temperature profiles are shown in Fig. 2.1.2. The diametral strain is low near the ends of the tube where the fast neutron flux is low, and peaks towards the outlet (hot) end.

An important factor affecting the shape of the diametral strain profile is the orientation of the coolant flow relative to the manufacturing direction of the pressure tube. Pressure tubes are made using hot-extrusion, followed by cold-drawing and heating in a steam autoclave at 673 K for 24 h [28]. In the hot-extrusion process the end of the tube emerging from the extrusion press first is referred to

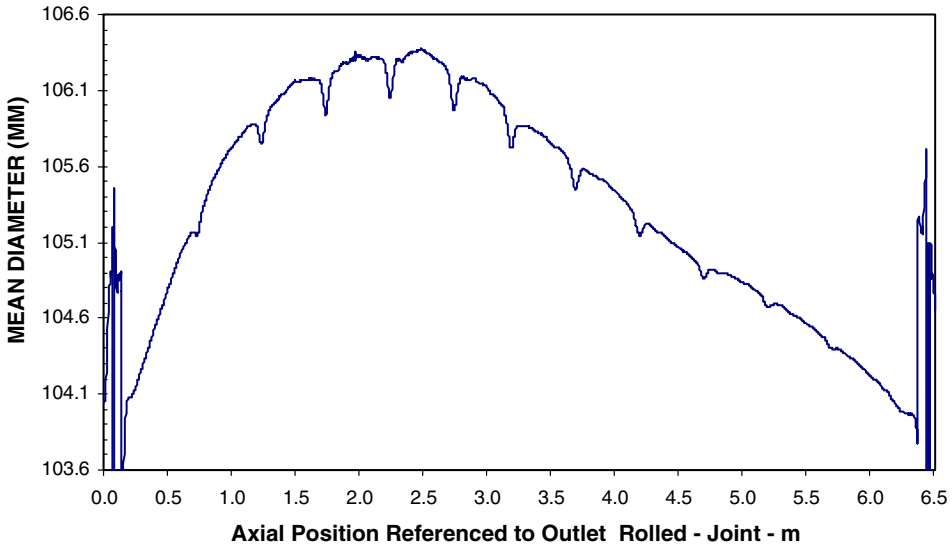

Fig. 2.1.1. Typical profile of diameter from outlet to inlet along the length of a CANDU 6 pressure tube.

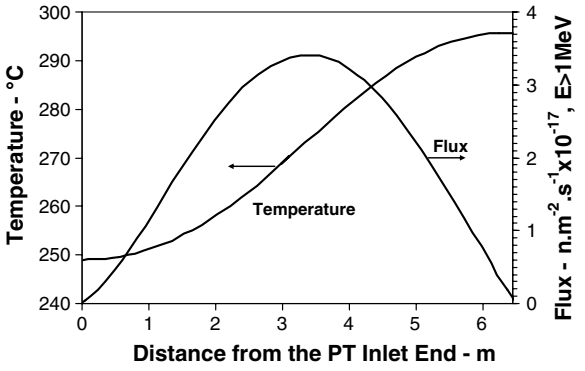

Fig. 2.1.2. Typical fast neutron flux and temperature profiles from inlet to outlet along a CANDU pressure tube.

as the 'front end' and the end emerging last is referred to as the 'back end'. The front ends of the tubes exhibit lower yield and ultimate tensile strengths than the back ends.

In earlier reactors the pressure tubes were always installed in the same geographic orientation relative to reactor core, e.g., the back end of the tube at the west end of the reactor. Since the coolant flow is in the reverse direction in alternating channels, half the pressure tubes then had their back ends at the outlet, and half had their back ends at the inlet. This resulted in two types of diametral strain profiles. Tubes with their back end at the outlet exhibited asymmetrical strain profiles like that shown in Fig. 2.1.1, and tubes with their back end at the inlet exhibited a more symmetrical strain profile, Fig. 2.1.3.

In later reactors tubes, were installed with their back ends at the outlet of all channels, to reduce the likelihood of a failure mechanism called delayed hydride cracking (DHC) at the rolled joints where the pressure tubes are joined to the steel end-fittings [29]. In the most recently built reactors, this concern has been alleviated and the tubes are installed with the back end at the inlet.

After a small positive transient, Fig. 2.1.4, the diametral strain rate at a given point along the pressure tubes appears to reach a steady state, and, unlike the situation for elongation, see Section 2.2, there is no evidence from power reactors that this rate changes with time throughout the life of the reactor. There is some suggestion from test reactor

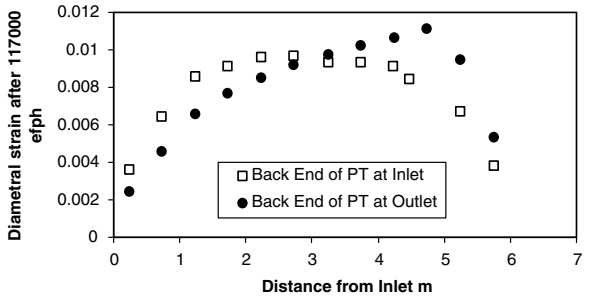

Fig. 2.1.3. Comparison of diameter profiles along CANDU pressure tubes with the back end at the inlet and the back end at the outlet, from Ref. [14].

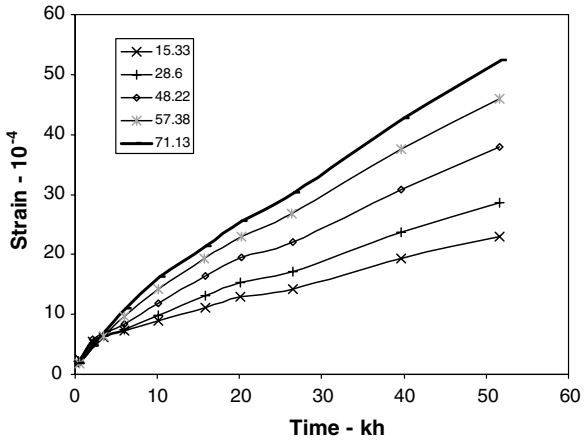

Fig. 2.1.4. Strain as a function of time for the fast neutron fluxes shown (in units of 10^{14} n m^{-2} s^{-1}, $E > 1$ MeV) showing an initial transient strain followed by a steady state rate, from Ref. [25].

experiments on small specimens [30] that the irradiation creep rate changes with fluence, and clear evidence that the growth rate does change [12], so reactor operators should remain vigilant.

The design of the fuel channels accounts for stress rupture/creep ductility and flow bypass. Based on data from in-reactor experiments, 5% is considered to be a very conservative limit with respect to creep rupture and creep ductility, Ells et al. [31], see Section 7. Although the measured diametral expansions are within the maximum value assumed in the analysis, lifetime management strategists are evaluating the need for increased inspections to precisely quantify the variability in expansion. This will allow more accurate assessments of effect of flow bypass on fuel cooling and the potential approach to fuel dry-out – the condition limiting the operating power of the reactor. The variability of diametral strain is also important because operating margin to fuel dry-out is based on the worst case. A new fuel design has been developed to ameliorate the effects of diametral creep on fuel cooling [32], which, if implemented, would delay any necessity to de-rate reactors as a result of degraded operating margins.

2.2. Axial elongation

Axial elongation is due to a combination of irradiation creep and irradiation growth [14,33]. Both of these phenomena are anisotropic, and result directly from the anisotropic crystal structure (hexagonal close packed or hcp) of zirconium, and the pronounced crystallographic texture produced during manufacturing. If Zr–2.5Nb were isotropic, there would be no significant pressure tube elongation. The designers of the earliest CANDU stations assumed that zirconium alloys were isotropic and made no allowance in the design for elongation beyond thermal and elastic expansion. Once pressure tube elongation was discovered, it was assumed that it would occur at a steady rate (several millimeter per year), after a short initial transient

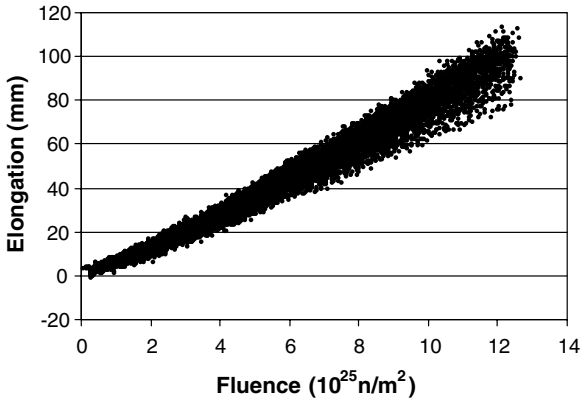

Fig. 2.2.1. Elongation as a function of fast neutron fluence (averaged along the length of each pressure tube) for a CANDU 6 reactor.

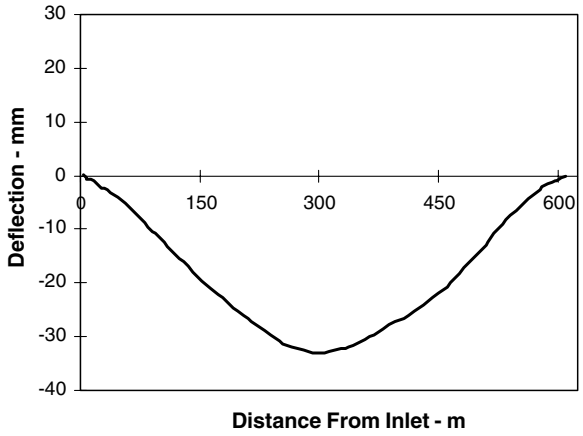

Fig. 2.3.1. Sag profile for a CANDU fuel channel after several years of operation.

[15], and much reactor maintenance is still planned based upon this assumption. However, it is now known that the elongation rate increases gradually with time [7,14], or more correctly with fast neutron fluence, Fig. 2.2.1. This increase in rate is attributed to evolution of the microstructure induced by the fast neutron flux [12].

Pressure tube elongation is accommodated by supporting the end-fittings on sliding bearings. One end is initially fixed and the other end is free to move outwards. About halfway through the design life, the channel is 'reconfigured', i.e., the free and fixed ends are reversed, allowing elongation to be accommodated at the other end of the reactor [7].

Two aspects of elongation are important: the magnitude and the differential between channels. Monitoring is necessary to establish the optimum time to reconfigure and to ensure deformation continues at the established rate. The difference in elongation rates between neighboring channels is also monitored so that interference between feeders or problems with fueling machine access do not occur. Recently, some progress has been made in understanding the sources of the variability in terms of the manufacturing variables and their effect on the microstructure [34].

Life management strategies currently involve measurement and calculation of the elongation rate of each channel to determine when maintenance is required. The fueling machine, in combination with specialized instrumentation, can be used to provide this elongation data on-line, see Fig. 2.2.1. The newest CANDU® stations have been designed with increased elongation margins to account for the gradual acceleration of the rate [7].

2.3. Sag

Sag occurs mainly by irradiation creep from the weight of the fuel and heavy water in the pressure tube, Fig. 2.3.1. Gross sag deformation is primarily controlled by the relatively cool calandria tube [18,19]. Sag of the pressure tube occurs between the spacers, but is only of consequence if spacers are sufficiently displaced from their design locations and the pressure comes in contact with the calandria tube. Fuel bundle passage, as proven by tests using predicted end of life curvature, is not impaired during the fuel channel design life [7].

In the design, sag is assessed to address the possibility of contact between the calandria tube and horizontal mechanisms that are perpendicular to the fuel channels: the liquid-injection-shutdown-system nozzles and horizontal-flux-detector-unit guide tubes [7]. Deformation predictions indicate that, although unlikely, such contact could occur before 30 years of reactor operation in earlier reactors. Measurements are planned on lead units to verify the calculations, and a modification is available to address the possibility that contact occurs. The newest units have more sag resistant calandria tubes, and greater clearances designed to accommodate the predicted sag with larger margins [7,35].

In early units, the loose-fitting spacer design was susceptible to movement during reactor assembly and early operation [29]. Because of the resulting wide span between some spacers, pressure tube to calandria tube contact could occur. This could lead to the potential for hydride blister formation and growth if the hydrogen concentration at the contact location exceeds the 'blister formation threshold' (BFT) [36]. A specialized spacer location and repositioning (SLAR) tool was developed to locate the spacers and relocate them, if necessary [37]. This maintenance operation is being carried out before BFT is reached. The operation is controlled by an operator using the computer code SLARON/SLARADE, Badie et al. [20], based on measured spacer locations and model calculations of the sag phenomenon. In 1983, the spacer design was changed from loose-fitting Zr–2.5Nb–0.5Cu to tight-fitting Inconel 600 spacers that do not move [38].

The models used to predict sag and control SLAR are still under development. These models are essential because the gross sag of the fuel channel is mainly controlled by the calandria tube, and hence sag measurements only give very crude information about the sag of the pressure tube per se.

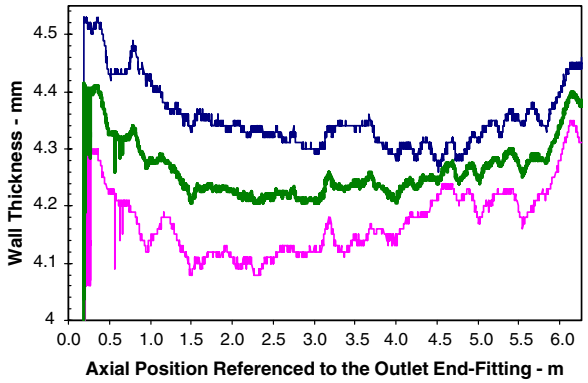

Fig. 2.4.1. Variation in wall thickness (maximum, average and minimum) of a CANDU pressure tube with distance from the outlet end-fitting.

The further development of these models and probabilistic assessment of the likelihood of contact are now probably the most important focus of on-going research.

2.4. Wall thinning

Creep and growth occur at constant volume, therefore the increase in diameter and length correspond to a reduction in the wall thickness. Sag also contributes a small amount to the loss of wall thickness on the side opposite the centre of curvature. A typical wall thickness profile at mid-life is shown in Fig. 2.4.1. The design of the fuel channels accounts for the stress increase both due to diametral expansion and due to wall thinning. Relative to the short term strength, increased stresses due to diametral expansion and wall thinning are more than offset by the radiation hardening that occurs during service. The recently developed capability to measure wall thickness profiles accurately, as shown in Fig. 2.4.1 allows a more accurate analysis of the diametral strain profiles and elongation with the possibility of detecting variations in anisotropy along the length of the pressure tube.

3. Microstructure and microchemistry of pressure tubes

The manufacturing route of Zr–2.5Nb pressure tubes has varied slightly between the construction of Pickering A (late 1960s) and Qinshan 1 and 2 (early 2000s), but the microstructure of the pressure tubes has remained reasonably consistent. The basic microstructure and crystallographic texture arise during the extrusion process (for summaries of the manufacturing route of pressure tubes see Refs. [28,39,40]). It comprises mainly hcp α-Zr grains that are highly elongated in the axial direction of the tube, as seen in the radial/axial plane, Fig. 3.1(a). In this view they are generally between 0.2 and 0.5 μm thick and several micrometer long. As seen in the radial/transverse plane there are three types of grains [41]. Usually they are a few micrometer wide, and are predominantly aligned in the transverse direction but often curl around, Fig. 3.1(b), and a few are aligned in the radial direction, Fig. 3.2(a). The elongated α-grains tend to be somewhat finer at the back ends of the tubes, Table 3.1 [22]. Occasionally, especially at the front ends of the tubes there are colonies of 'misaligned' α-grains, which result from the β- to α-phase transformation during cooling after extrusion, Fig. 3.2(b) [40]. The α-grains contain 0.6–1.0%Nb, a slightly super-saturated solid solution which is thermally stable because the transformation kinetics are sluggish [42].

Between many of the α-grains, there is a thin film of 'β-phase', perhaps 20–50 nm thick, see Figs. 3.1 and 3.2. After extrusion, this phase is metastable body centred cubic (bcc) β-Zr containing approximately 20%Nb, but after cold-work and autoclaving, this phase has partially transformed, through a complicated sequence, towards the equilibrium phase distribution of α (<0.5%Nb) and bcc β-Nb (~95%Nb) and contains a combination of ω (a metastable hcp phase of intermediate Nb content) and β-Zr enriched in Nb to ~50% [43]. This partial transformation is recognizable by the internal structure of the β-phase observed after autoclaving, but not immediately after extrusion, Fig. 3.3.

Oxygen, which is deliberately controlled to give short term strength [28] is concentrated in the α-phase and depleted in the β [40], although there is no technique that will give a quantitative assessment on such fine microstructures. The major impurity in Zr–2.5Nb is Fe which is a β-stabilizer in Zr, and is primarily concentrated in the β-phase. Fe is also found at the α–α grain boundaries [44].

The dislocation structure in the α-phase arises mainly from the cold-drawing process (~27% reduction in area), and subsequent recovery during autoclaving [45]. It comprises both **a** dislocations, i.e., dislocations with a Burgers vector lying in the basal plane of the hcp crystal, and **c**-component dislocations, i.e., dislocations with a component of their Burgers vector normal to the basal plane. The two types can be observed by transmission electron microscopy, Fig. 3.4 [46]. Using X-ray diffraction [47] the total dislocation is estimated as $3\text{–}4 \times 10^{14}\ \mathrm{m}^{-2}$. and typically the **c**-component dislocation density is 10–20% of the total [22].

The anisotropic nature of the in-reactor deformation processes in pressure tubes results predominantly from the anisotropic hcp α-Zr crystal structure and the crystallographic texture developed during the extrusion process. The anisotropy is mainly controlled by the orientation of the **c**-axis, or basal plane normal. This is the strong direction of the crystal [48]. A typical basal pole figure for a pressure tube is shown in Fig. 3.5. The basal plane normals are distributed in the radial/transverse plane and concentrated predominantly in the transverse direction [28]. This concentration tends to be higher at the front ends of the tubes. Often there is a small concentration of basal plane normals in the axial direction of the tube at the front end associated with the presence of colonies of misaligned α-grains [49], mentioned above. The basal plane texture is often quantified by F_R, F_T and F_A, the resolved fractions of basal plane normals in the radial, transverse and axial

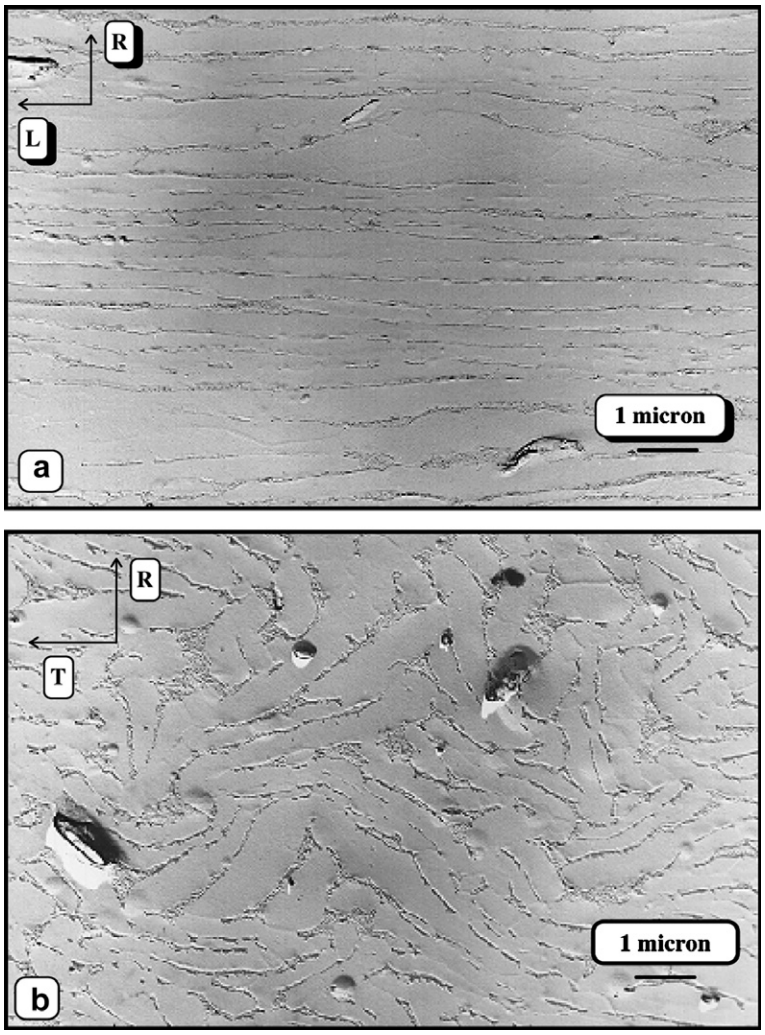

Fig. 3.1. Transmission electron micrographs from carbon replicas of a pressure tube showing: (a) elongated α-grains in the axial/radial section and (b) curved flattened α-grains in the radial/transverse section, from Ref. [41].

directions, respectively [50]. These quantities represent a normalized average of a second-order tensor resolution into the tube directions of dilations along the **c**-axis for all crystallographic orientations [51]. Typical values for pressure tubes are given in Table 3.1 [22].

Unless otherwise specified, the deformation characteristics described below pertain to material with the microstructural characteristics given above, and to operating conditions that are representative of the behaviour of pressure tubes in power reactors.

4. Variability of pressure tube deformation

Within one reactor, the deformation rates of pressure tubes can vary substantially once temperature, fast neutron flux and tube orientation have been taken into account. In the case of elongation, this variation is of the order of ±15–20% [33] and in the case of diametral strain the variation can be of the order of ±30% [22]. Further variations are seen from reactor to reactor, but these might be attributable to differences in operating conditions. A number of correlations have been established between the overall diametral strain [22] and elongation [34] of pressure tubes and microstructural, chemical and manufacturing information.

The elongation rate of pressure tubes shows a decrease with increasing Fe concentration, Fig. 4.1 [52]. A similar correlation is seen between the rate of irradiation growth and Fe concentration, Section 5.4. The elongation rate also appears to vary from one ingot to the next [53], Fig. 4.2, which could be attributable to ingot chemistry, or could be a manufacturing batch effect [34].

The diametral strain rate decreases with grain thickness, Fig. 4.3, decreases as the distribution of basal plane normals becomes more pronounced in the transverse direction, Fig. 4.4, and decreases as the oxygen concentration (as analysed in the ingot) increases, Fig. 4.5 [22].

In all cases these correlations may be misleading because there are many potentially confounding variables.

The effect of grain size might be expected from the theoretical predictions of the effect of grain size on irradiation growth in the transverse direction [54], see Section 5.6. The effect of texture is expected from its effect on both creep

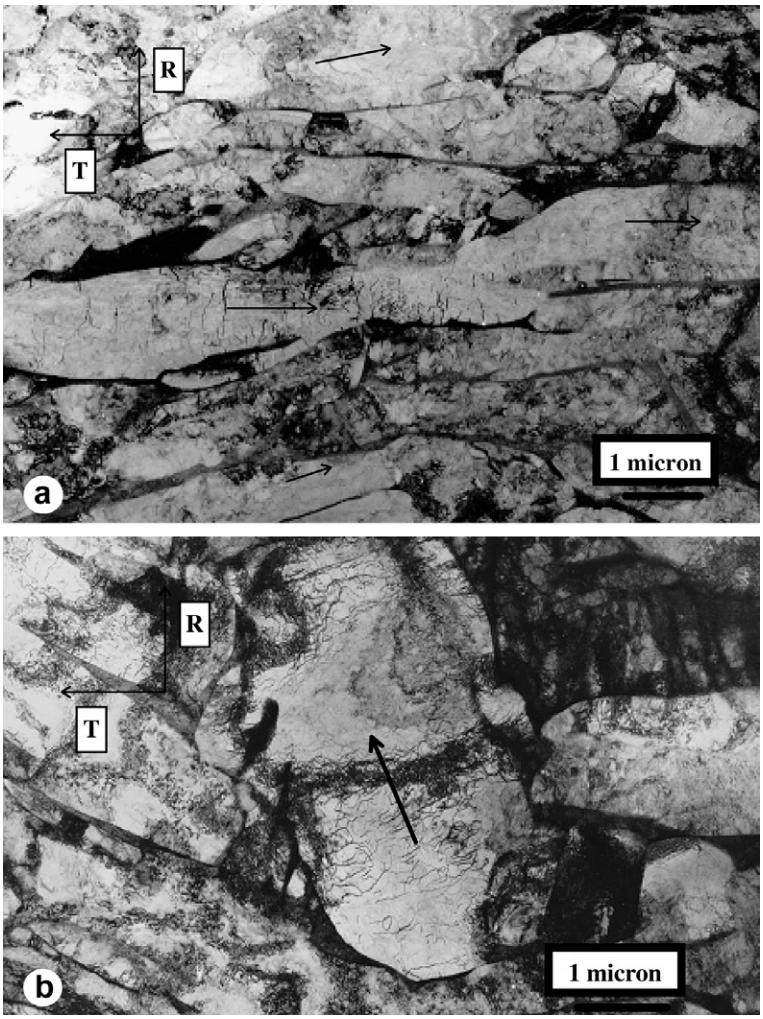

Fig. 3.2. Transmission electron micrographs from thin foils of a pressure tube showing: (a) transversely oriented α-grains in the radial/transverse section and (b) a radially oriented α-grain in the radial/transverse section. Both micrographs show some Widmanstätten α-grains (centre in (a) and upper right in (b)), from Ref. [41].

Table 3.1
Front-to-back variation in microstructural parameters for pressure tubes (±1 standard deviation)

Parameter	Front	Back
F_R	0.298 ± 0.025	0.350 ± 0.029
F_T	0.642 ± 0.031	0.605 ± 0.032
F_L	0.057 ± 0.017	0.05 ± 0.05
Grain thickness (μm)	0.45 ± 0.08	0.34 ± 0.06

and growth [55]. The effect of O concentration could be related to the solid solution strengthening effect of O in Zr [56], or the effect of O on the phase distribution during extrusion which could, in turn affect the texture. The effect of Fe on elongation may be related to its effect on growth.

5. Irradiation growth

Irradiation growth is a shape change induced by any energetic radiation that causes displacement damage – displacement of atoms from their normal position – in the absence of applied stress. There is no volume change – a radiation-induced shape change accompanied by a volume increase is referred to as irradiation-induced swelling, and is not significant in zirconium alloys at the temperature of operation of thermal reactor components. Irradiation growth is relatively easy to study by measuring the dimensional changes of unstressed specimens as a function of irradiation time, or fast neutron fluence. The irradiation growth of Zr–2.5Nb pressure tube materials at 525–585 K – the operating temperature range of CANDU pressure tubes – depends upon their initial microstructure – crystallographic texture, grain size, dislocation density – fast neutron flux, temperature, fast neutron fluence (which induces changes in the dislocation structure) and chemical composition.

5.1. Effect of fast neutron fluence

The growth behaviour of Zr–2.5Nb pressure tube material in the axial and transverse directions at 550 K is

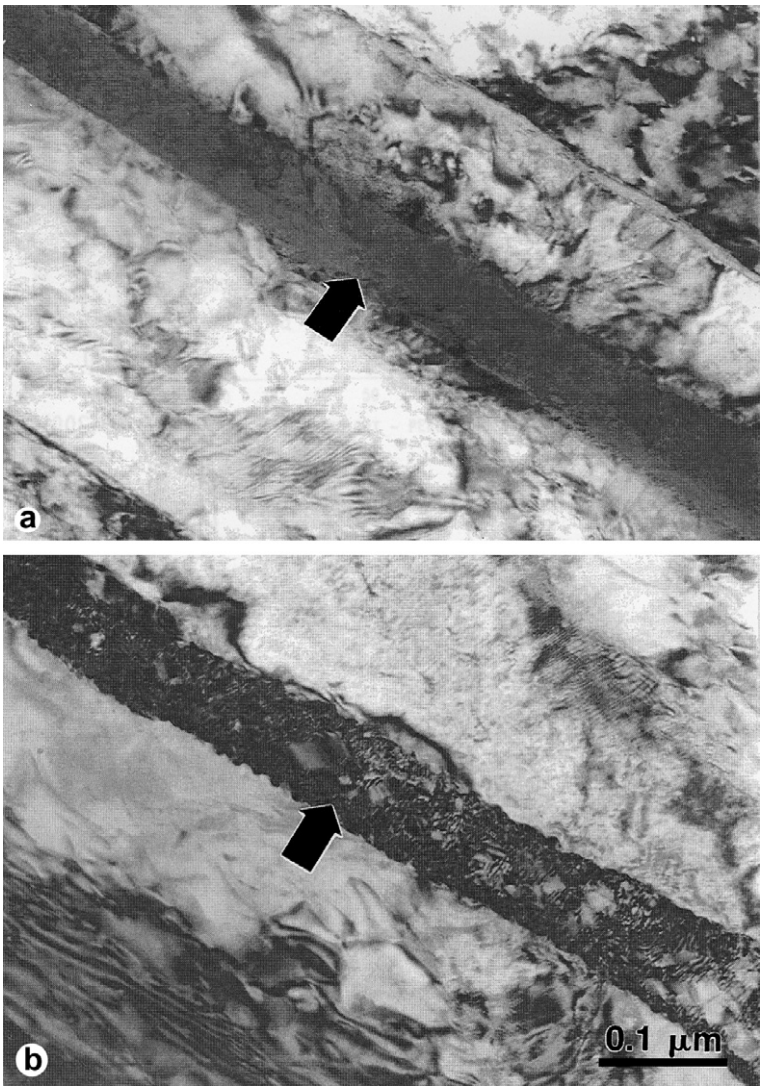

Fig. 3.3. Transmission electron micrographs from thin foils of a pressure tube showing: (a) undecomposed β-phase before autoclaving and (b) partially decomposed β-phase after autoclaving for 24 h at 673 K, both in radial/axial section, from Ref. [43].

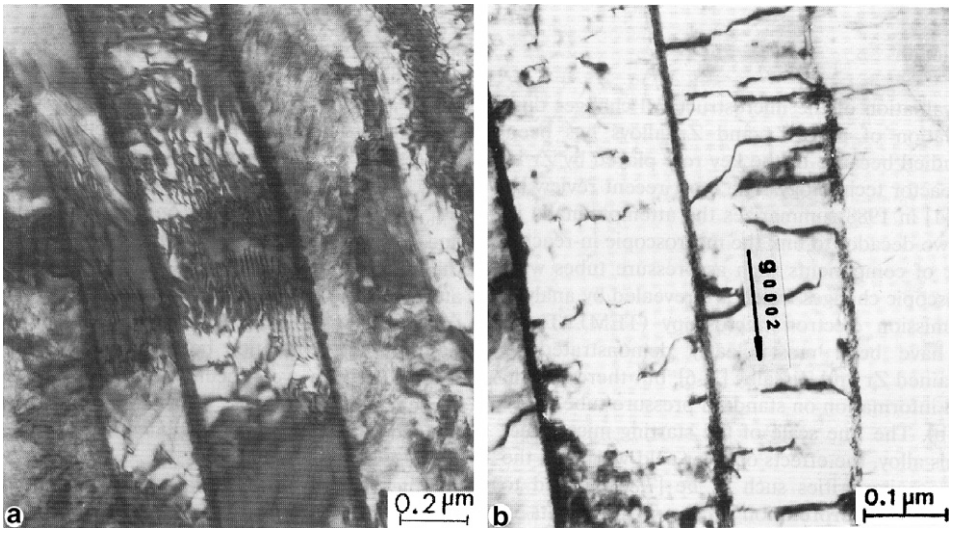

Fig. 3.4. Transmission electron micrographs from thin foils of a pressure tube showing: (a) **a**-dislocations ($\mathbf{b} = 1/3\langle 11\bar{2}0\rangle$) and (b) **c**-component dislocations ($\mathbf{b} = 1/3\langle 11\bar{2}3\rangle$), both in radial/transverse section, from Ref. [46].

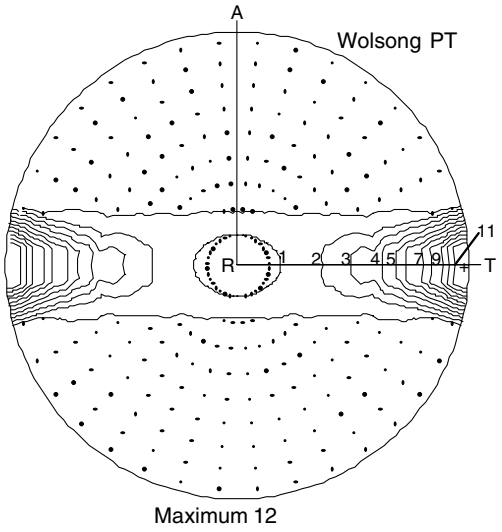

Fig. 3.5. Typical basal pole figure of a cold-worked Zr–2.5Nb pressure tube, from Ref. [17].

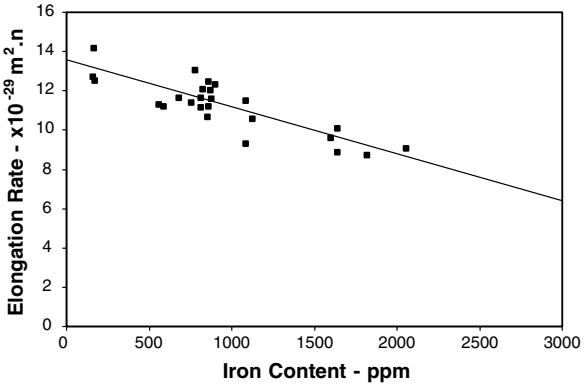

Fig. 4.1. Correlation of in the elongation rate of pressure tubes in a CANDU reactor with the ingot iron analysis, from Ref. [52].

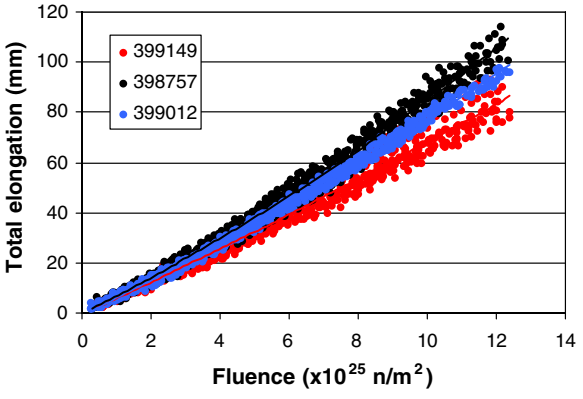

Fig. 4.2. Elongation as a function of fast neutron fluence (averaged along the length of each pressure tube) for tubes made from three different ingots in a CANDU 6 reactor.

illustrated for low and high fast neutron fluence in Figs. 5.1.1 [57,58] and 5.1.2 [12]. There is an initial rapid increase in length in the axial direction and decrease in length in the

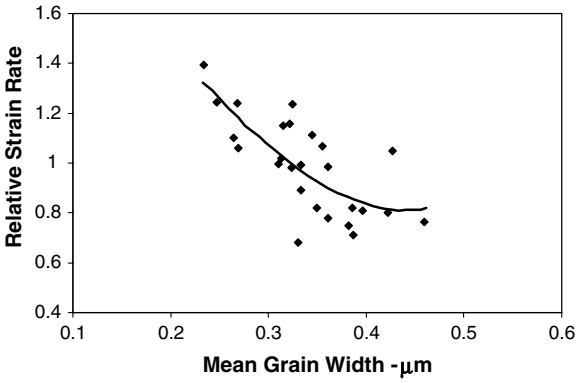

Fig. 4.3. Correlation between peak diametral strain rate of pressure tubes in operating reactors and grain thickness, from Ref. [22].

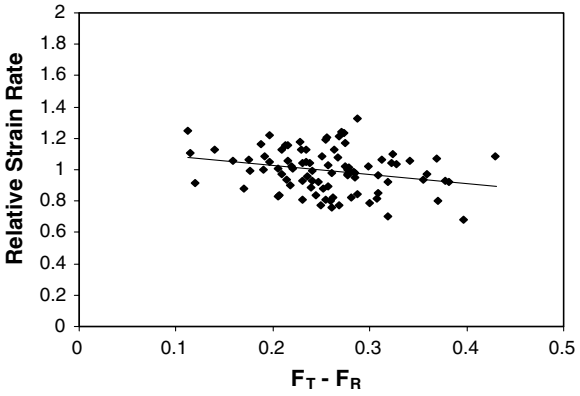

Fig. 4.4. Correlation between peak diametral strain rate of pressure tubes in operating reactors and the difference between texture parameters $F_T - F_R$, from Ref. [22].

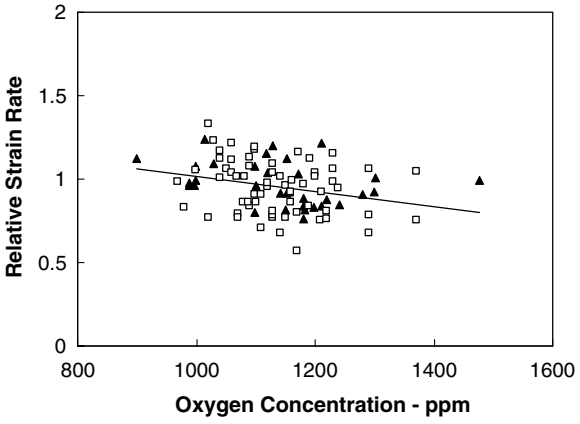

Fig. 4.5. Correlation between peak diametral strain rate of pressure tubes in operating reactors and the ingot oxygen analysis for two reactor types, from Ref. [22].

transverse direction of about 0.02%. Subsequently, the growth is relatively flat, or slightly negative in the axial direction for a fast fluence of $1–1.5 \times 10^{25}$ n m^{-2}, $E > 1$ MeV, and establishes a relatively steady negative rate in the transverse direction after about 0.5×10^{25} n m^{-2},

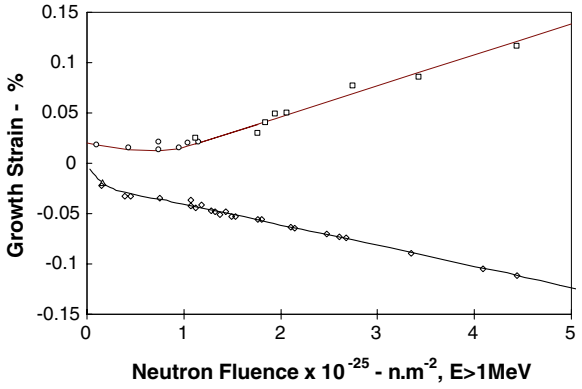

Fig. 5.1.1. Growth strain as a function of fast neutron fluence for cold-worked Zr–2.5Nb in DIDO at a fast neutron flux of $\sim 6 \times 10^{17}$ n m^{-2} s^{-1}, $E > 1$ MeV, from Ref. [58].

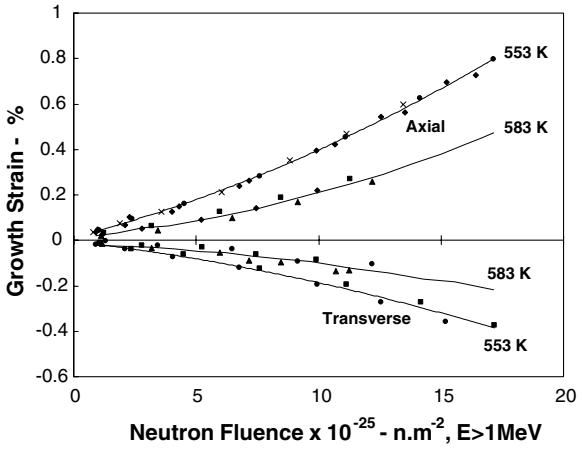

Fig. 5.1.2. Growth strain as a function of fast neutron fluence for cold-worked Zr–2.5Nb in Osiris at a fast neutron flux of $\sim 2 \times 10^{18}$ n m^{-2} s^{-1}, $E > 1$ MeV, from Ref. [12].

$E > 1$ MeV. After these initial transients, growth is typically positive in the axial direction of the tube, and negative in the transverse direction. The magnitude of growth in the transverse direction is approximately half that in the axial direction.

In the longer term, the growth rate gradually accelerates in both directions and after a fast neutron fluence about 2×10^{25} n m^{-2}, $E > 1$ MeV, the behaviour is reasonably well described by a quadratic equation. The acceleration continues, but remains gradual until fast fluences of at least 2.4×10^{26} n m^{-2}, $E > 1$ MeV [12], i.e., approaching those experienced over their design life by CANDU pressure tubes. The rate changes can be related to the changes in dislocation structure with fluence [12], in particular an increase in the density of **c**-component dislocations, see Sections 9 and 10.

Often, the rate is assumed to be linear over the later part of the fluence range and growth 'rates' are compared on this basis. Measurements of the growth of compact toughness specimens in three dimensions at about 520 K, has confirmed that there is negligible volume change, so that

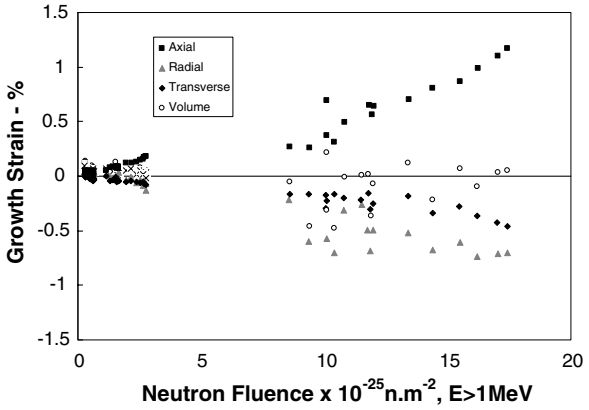

Fig. 5.1.3. Growth strains in three dimensions as a function of fast neutron fluence for Zr–2.5Nb pressure tube material irradiated at 520 K in Osiris at $\sim 2 \times 10^{18}$ n m^{-2} s^{-1}, $E > 1$ MeV, from Ref. [59]. Note several points in the range 9–13 $\times 10^{25}$ n m^{-2} are thought to be erroneous.

the strain rates in all three directions evolve with fast fluence, Fig. 5.1.3 [59], and the strain in the thickness direction can be inferred to be the negative sum of the strains in the axial and transverse directions.

5.2. Effect of fast neutron flux

Above a certain temperature, the irradiation growth strain rate is approximately proportional to the effective displacement damage rate, i.e., the rate at which atoms are displaced from their lattice positions by the fast neutrons. Linear flux dependence is demonstrated by the irradiation of similar materials at different flux levels. There is a complication in that different irradiation facilities may have different flux spectra, and therefore different degrees of effectiveness at producing displacement damage. There are no good data on flux dependance for Zr–2.5Nb pressure tube materials at 525–585 K, and there is a significant discrepancy between data obtained in the DIDO reactor in the UK and the Osiris reactor in France [52]. However, when normalized for flux spectrum, the Osiris data agree well with data for specimens irradiated in CANDU in a 'carrier bundle' specifically designed for the purpose of irradiating small specimens in power reactors, Fig. 5.2.1 [60], so it appears that the flux dependence is indeed approximately linear. Also, it has been clearly demonstrated that the flux dependence is linear at 330–350 K for cold-worked Zircaloy-2 pressure tube material irradiated in the ATR Reactor in the US at 2–4 $\times 10^{18}$ n m^{-2} s^{-1}, $E > 1$ MeV, and in DIDO in at a flux of about 1/4 of that [55]. Theoretically, a linear flux dependence at this temperature always implies a linear flux dependence at higher temperatures [54], see Section 10.

Linear fast flux dependence appears to be a consequence of the partitioning of the point defects created by the displacement damage amongst various 'sinks' in the microstructure with little recombination, see Section 10. The implication of a linear fast flux dependence is that growth

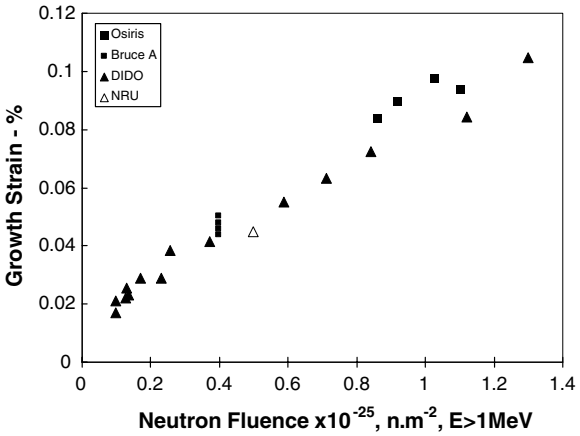

Fig. 5.2.1. Growth strain in the axial direction of cold-worked Zircaloy-2 pressure tube material at 553 K in DIDO at $\sim 6 \times 10^{17}$ n m^{-2} s^{-1}, $E > 1$ MeV; 553 K in Osiris at $\sim 2 \times 10^{18}$ n m^{-2} s^{-1}, $E > 1$ MeV, and in a carrier bundle in a CANDU reactor at $\sim 2 \times 10^{17}$ n m^{-2} s^{-1}, $E > 1$ MeV, from Ref. [60].

strain can be plotted vs fast fluence, independent of the fast flux – an almost universal practice. The deformation rate is then expressed in units of m^2 n^{-1}, $E > 1$ MeV.

5.3. Effect of temperature

Typical irradiation growth curves for pressure tube materials at 553 and 583 K are shown in Fig. 5.1.2, in which the magnitudes of the positive axial and negative transverse growth strains both decrease with increasing temperature. Over a temperature range of 330–623 K, the growth rate of Zr–2.5Nb pressure tube material in the axial direction decreases with temperature, Fig. 5.3.1 [58,61,62]. Over the temperature range of pressure tube operation, the same behaviour is seen for a variety of different pressure tube materials, Fig. 5.3.3, the curves being displaced for materials with different Fe concentrations (see Section 5.4). The (negative) magnitude of the transverse growth rate also decreases with temperature, for a range of tubes,

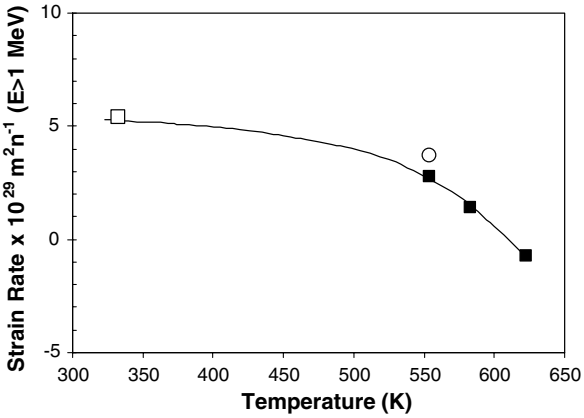

Fig. 5.3.1. Effect of temperature on the growth rate of cold-worked Zr–2.5Nb pressure tube material, from Ref. [61].

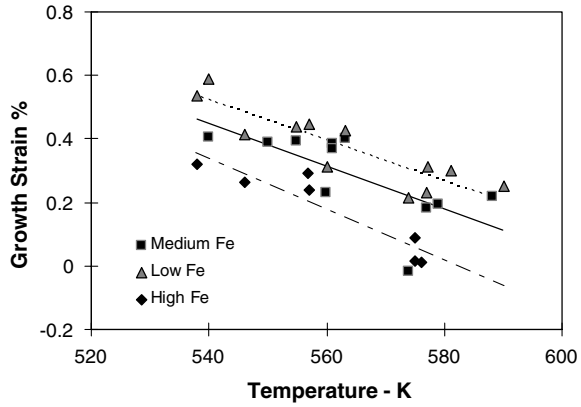

Fig. 5.3.2. Growth strain in the axial direction of cold-worked Zr–2.5Nb pressure tube material at a fast neutron fluence of 1×10^{26} n m^{-2}, $E > 1$ MeV, as a function of temperature, from Ref. [12].

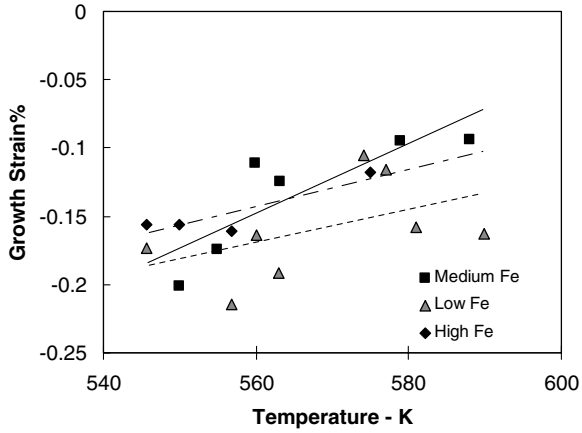

Fig. 5.3.3. Growth strain in the transverse direction of cold-worked Zr–2.5Nb pressure tube material at a fast neutron fluence of 1×10^{26} n m^{-2}, $E > 1$ MeV, as a function of temperature, from Ref. [12].

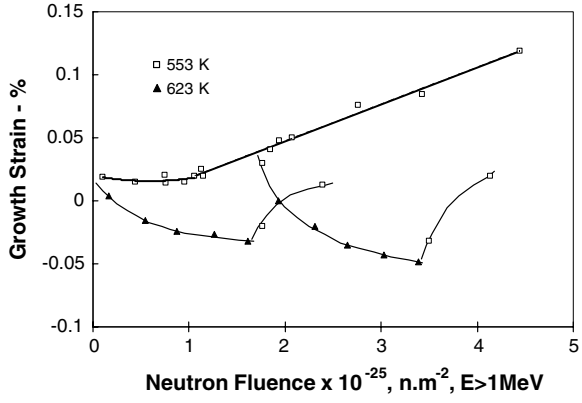

Fig. 5.3.4. Growth strain as a function of neutron fluence showing the effects of temperature changes between 553 K and 623 K for cold-worked Zr–2.5Nb pressure tube material irradiated in DIDO at $\sim 6 \times 10^{17}$ n m^{-2} s^{-1}, $E > 1$ MeV, from Ref. [58].

Fig. 5.3.4. When the parameters of quadratic equations fitted individual growth curves are plotted as a function of

temperature, it appears that the temperature affects primarily the initial growth rate, but has less effect on the rate of acceleration.

When the temperature is changed during a growth test, there are significant transients, Fig. 5.3.4, and the growth rate does not immediately re-establish itself at the expected rate for the new temperature [58]. Analysis of the anisotropy of these transients suggested that there may be a long lasting effect of the dislocation microstructure developed at the earlier irradiation temperature. This could be important in future reactors that are designed to load follow with significant changes in temperature over the power range.

5.4. Effect of Fe concentration

Based on the fact that Fe has a significant effect on the diffusional characteristics of vacancies in Zr [63,64], and the observation that the elongation rates of pressure tubes correlate with Fe concentration (see Section 4), pressure tubes with different Fe concentrations were chosen for a long term growth experiment in the Osiris reactor in France [12,52]. These showed a clear trend, with the magnitude of the irradiation growth rate in either direction decreasing with increasing Fe concentration. Fig. 5.4.1 shows growth curves for pressure tube materials at a nominal temperature of 553 K with two different Fe concentrations. Fig. 5.3.3 shows the effect of Fe on the axial growth rate as a function of temperature, and Fig. 5.3.4 the effect of Fe on the transverse growth rate as a function of temperature. As in the case of temperature, the initial rate is more sensitive to Fe concentration than the acceleration in the growth rate with increased fluence, Fig. 5.3.4. The effect of Fe has not yet been satisfactorily explained. During irradiation it is dispersed into the α-phase [44], but whether it remains in solution or exists as sub-microscopic precipitates is not known. As a solute, it may affect the vacancy diffusion characteristics [63], while as a precipitate, it might provide recombination sites for vacancies and interstitials. Also, its presence at α–α grain boundaries [44] could influence their role as sinks. Finally, Fe changes the volume fractions of α and β during extrusion, and could thus have an indirect influence through the texture.

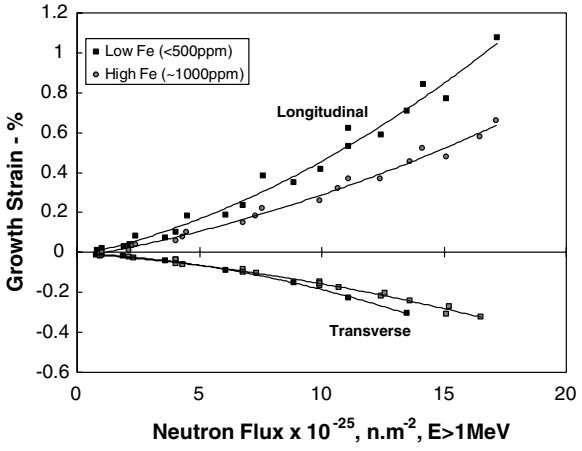

Fig. 5.4.1. Growth strain as a function of fast neutron fluence for cold-worked Zr–2.5Nb with different Fe contents in Osiris at a fast neutron flux of $\sim 2 \times 10^{18}$ n m^{-2} s^{-1}, $E > 1$ MeV.

5.5. Effect of crytallographic texture

Based on the growth behaviour of a typical pressure tube material, Section 5.1, it can easily be inferred that, on the crystalline level, growth comprises, to some degree, shrinkage along the **c**-axis and expansion along the **a**-axis of the hcp crystal. Growth tests on small diameter tubes with two different crystallographic textures irradiated to high fast neutron fluence in the Osiris reactor in France clearly illustrate this [17]. Fig. 5.5.1 shows the crystallographic textures of the two types of tubes referred to as FS (fuel sheathing) and MPT (micro-pressure tube), and Table 5.5.1 gives the microstructural parameters. Fig. 5.5.2 illustrates the growth behaviour in two directions for both types of tubes at 553 K. Both FS and MPT material grow a similar amount in the axial direction, in which there are very few basal plane normals. The MPT material exhibits a much greater shrinkage in the transverse direction than FS material, corresponding to the much higher concentration of basal plane normals in the transverse direction in MPT material than in FS material.

At the single crystal level, this behaviour corresponds to a net accumulation of vacancies at defects (dislocations, dislocation loops) lying on the basal plane and an accumulation of self-interstitial atoms (SIAs) at defects perpendicular to the basal plane, as originally proposed by Buckley [65]. As seen in the next section, however, there are other components to the behaviour which is clearly modified by very fine elongated grain structures. In addition, we now know that the dislocation structures in different crystal orientations is different [12] and this will no doubt affect the growth anisotropy [66].

5.6. Effect of dislocation density and grain size

There are no growth data for Zr–2.5Nb pressure tube material in which the initial dislocation density[2] has been varied independently of other parameters – notably the grain size and the condition of the β-phase. Similarly, there is no growth data for which the grain size has been varied independently of other parameters. The work on Zircaloy-2 and Zircaloy-4 [55] has clearly demonstrated that the growth rate increases approximately linearly with increasing dislocation density, and also probably depends upon the types of dislocations present (**a**-type vs **c**-component), and whether or not the material has been stress relieved. Growth rates of Zircaloy-2 and Zircaloy-4 pressure tubes

[2] Here, we are referring to the dislocation density of the material prior to irradiation, e.g., due to cold-work, and not the dislocation structure induced by irradiation, as discussed in Section 9.

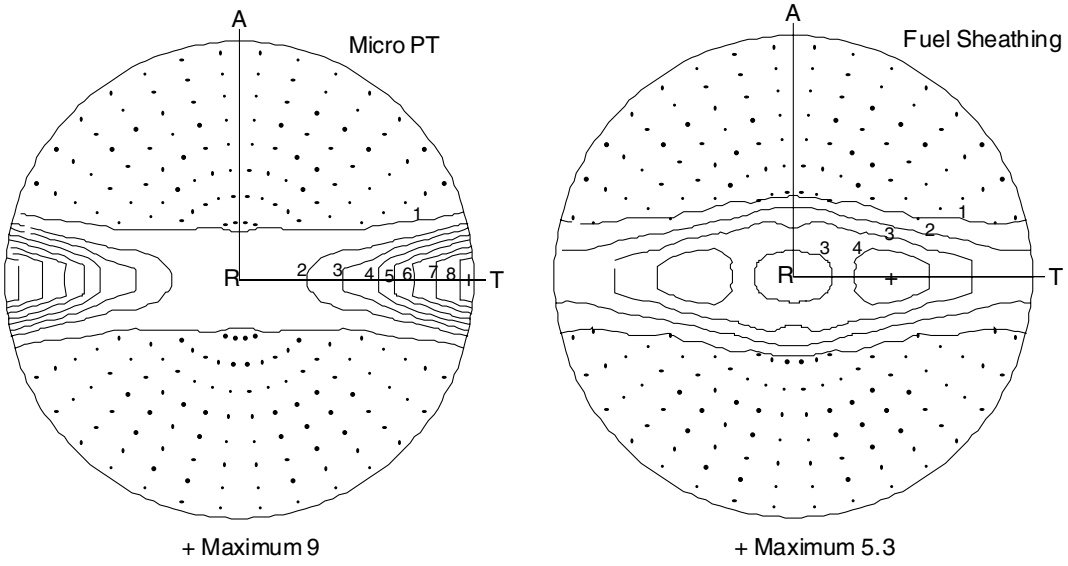

Fig. 5.5.1. Basal pole figures for small tubes irradiated in Osiris, from Ref. [17].

Table 5.5.1
Microstructural parameters for Zr–2.5Nb fuel sheathing and micro-pressure tubes irradiated in Osiris

Parameter	Fuel sheathing	Micro-pressure tube
a-type dislocation density	2.3×10^{14} m^{-2}	3.4×10^{14} m^{-2}
c-component dislocation density	0.6×10^{14} m^{-2}	0.7×10^{14} m^{-2}
F_R	0.57	0.34
F_T	0.37	0.57
F_L	0.07	0.09

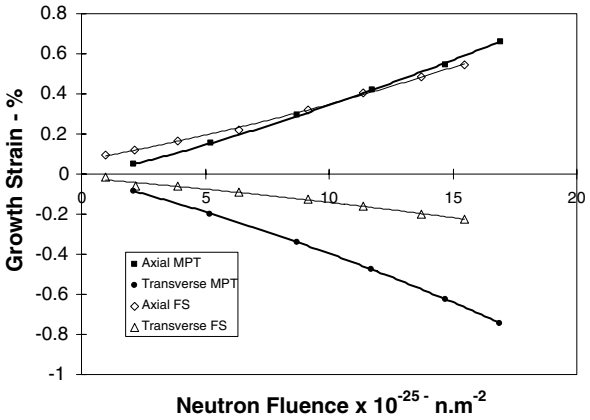

Fig. 5.5.2. Growth strains for small tubes with two different crystallographic textures irradiated at 553 K in Osiris at a neutron flux of $\sim2\times10^{18}$ n m^{-2} s^{-1}, $E>1$ MeV, from Ref. [17].

derived from the total strain in power reactors also varied approximately linear with dislocation density [67]. Grain size, per se (typically in the range >5 μm for the Zircaloys), appeared to have little effect, but the anisotropy of growth was also inferred to depend upon the grain shape.

A deliberate attempt to take advantage of these characteristics was made with the development, in the early 1980s of modified pressure tube manufacturing routes, referred to as the Task Group 3 (TG3) program [39,57,58]. In this program, pilot orders of pressure tubes were made with the target of modifying the grain shape, grain size and dislocation density. In addition standard pressure tube materials were modified by cold-working and heat treatment to change the dislocation density and grain size. Irradiation growth tests were carried out to fluences of 6–8×10^{25} n m^{-2}, $E>1$ MeV [58], Table 5.6.1. Of seven materials tested, seven had a grain size between 0.31 and 0.37 μm – within the typical range for pressure tubes, with dislocation densities varying between 1.7 and 4.8×10^{14} m^{-2}. These show an approximate linear dependence upon the dislocation density, Fig. 5.6.1. It should be kept in mind that other variables (e.g., the degree of transformation of the β-phase) may be at play.

In one case, referred to as TG3 R1, the dislocation density was reduced to 2.4×10^{14} m^{-2} by a high temperature stress-relief, and the corresponding reduction in tensile strength compensated for by reducing the grain size to 0.27 μm. This resulted in an irradiation growth rate that was actually negative in the axial direction while still remaining negative in the transverse direction, Fig. 5.6.2 [58,62]. If the growth rate data are corrected to a dislocation density of 4×10^{14} m^{-2} using the slope of Fig. 5.6.1, and adjusted to a grain aspect ratio of 15:1 and an F_A of 0.03 using the growth anisotropy factor described in [54], the grain size sensitivity can be plotted, Fig. 5.6.3. This shows a very rapid increase from negative to positive growth rates between 0.27 and 0.31 μm, followed by a saturation between 0.37 and 1.5 μm. Again there may be other factors at play, but both Figs. 5.6.1 and 5.6.3 are remarkably similar to the theoretical curves for the sensitivity of axial growth to dislocation density and grain size [54], see Section 10.

Table 5.6.1
Microstructural details and long term irradiation growth rates at 553 K of Zr–2.5 Nb pressure tube materials modified to vary grain size, grain shape and dislocation density [61]

Material designation	Dislocation density ($\times 10^{14}$ m^{-2})	F_R	F_T	F_A	Grain aspect ratio[a]	Grain thickness[a] (μm)	Axial growth rate[b]	Transverse growth rate[b]
AR	4.2	0.36	0.61	0.03	15–20	0.32	3.2	–
SR	1.8	0.36	0.61	0.03	15–20	0.32	0.8	–
CW	4.7	0.28	0.64	0.08	2.3	1.5	3.7	–
R1	2.4	0.40	0.56	0.03	15–20	0.25	−2.1	−0.7
R2	4.8	0.37	0.59	0.03	5–10	0.34	3.2	−1.4
R3	2.7	0.36	0.61	0.03	5–10	0.37	2.3	−1.5
D1	4.5	0.35	0.62	0.04	15–20	0.31	2.7	−2.2

[a] Grain length in the axial direction/grain thickness in the radial direction.
[b] Averaged in units of 10^{29} m^2 n^{-1} between 2 and 8×10^{25} n m^{-2}, $E > 1$ MeV.

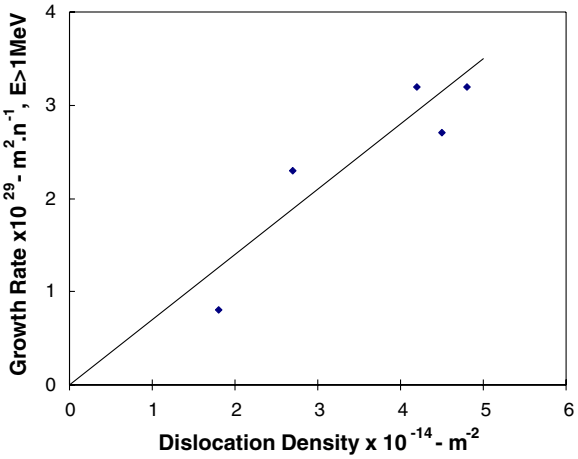

Fig. 5.6.1. Effect of dislocation density on growth rate for cold-worked Zr–2.5Nb with a grain thickness of 0.31–0.37 μm.

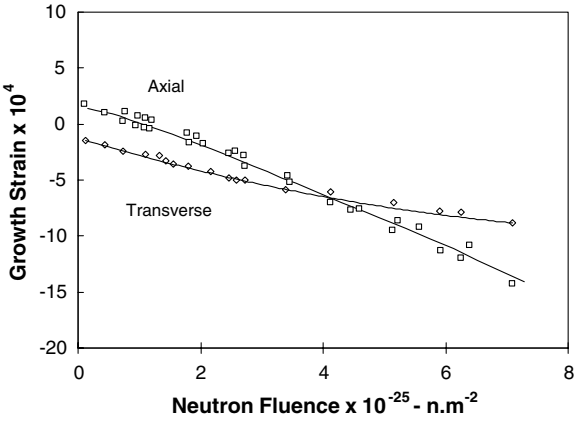

Fig. 5.6.2. Growth strain as a function of neutron fluence for modified pressure tube material with a low dislocation density and fine grain size. Irradiated in DIDO at 553 K and $\sim 6 \times 10^{17}$ n m^{-2} s^{-1}, $E > 1$ MeV, from Ref. [61].

Curiously, there is no discernable effect of pre-extrusion β-quenching of the material [52], an operation expected to refine the grain size. No microstructural data were reported, and possibly the tubes studied had grain sizes

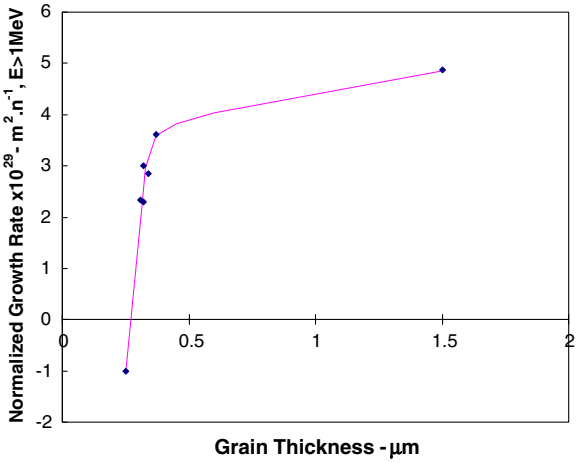

Fig. 5.6.3. Effect of grain thickness on the growth rate for cold-worked Zr–2.5Nb corrected to a dislocation density of 4×10^{14} m^{-2}, to a grain aspect ratio of 15:1 and an F_A of 0.03.

in the range 0.3–0.5 μm, where the effect of grain size is small and other factors dominated.

5.7. Effect of residual stress

Intergranular residual stresses are developed in Zr alloys during heating and cooling (as a result of the anisotropic thermal expansion of the hcp crystal), and during deformation as a result of plastic anisotropy [68,69]. In Zircaloy-2 these have been shown both theoretically and experimentally to result in long term transient irradiation growth response whose sign and magnitude depend in a sensible way upon the prior thermal or mechanical treatment [68–70]. The transient irradiation growth strain observed in the first 2×10^{25} n m^{-2}, $E > 1$ MeV, Fig. 5.1.1, may well be attributable to the relaxation of such stresses [71].

6. Irradiation creep

Irradiation creep is more difficult to study than irradiation growth because any shape change that occurs under an applied stress incorporates some components of the shape change that occurs without stress or due to thermal creep.

For practical purposes, the irradiation growth strain is simply subtracted from the total strain, the difference being defined as 'creep'. However, on a microscopic level, the processes associated with the 'growth' strain may be different with and without stress depending upon the mechanism (see Section 10). The issue of the thermal creep is even more complicated because the creep rate without a fast neutron flux is not relevant to the in-flux behaviour, since it is suppressed by radiation damage [14,15,25] as will be discussed in Section 7.2. Frequently, it is found that the latter is small relative to the radiation-induced component of creep and in many cases, to a first approximation, can be ignored.

6.1. Effect of fast flux

The dependence of irradiation creep of Zr alloys on fast neutron flux (displacement damage rate) is often expressed as a power law, i.e.,

$$\dot{\varepsilon}_{ic} \propto \phi^n, \tag{6.1.1}$$

where ϕ is the fast neutron flux and n is the 'flux exponent'.

For pressure tubes at reactor operating temperatures the fast flux dependence is generally accepted to be approximately linear, i.e., $n \sim 1$ [15].

Although no similar experiments exist for Zr–2.5Nb, the linear sensitivity of irradiation creep to displacement damage has been clearly demonstrated by proton irradiation in hot-rolled and annealed Zircaloy-2 plate at 553 K [72], Fig. 6.1.1.

The effect of fast flux is most graphically demonstrated for Zr–2.5Nb pressure tubes by the diametral strain profiles of pressure tubes in power or test reactors, and examples of which are shown in Fig. 2.1.3. Here the strain follows the profile of the fast flux through the core (although these may be skewed because of the temperature gradient and/or end-to-end effect). The diametral strain includes a component of growth which also has a linear dependence on fast flux (Section 5.2) and also includes thermal creep. Note that if thermal creep were a significant contributor to the total strain rate (e.g., as the temperature increases) the total strain rate would exhibit a flux exponent, $n < 1$ even when the flux dependence of irradiation creep was linear.

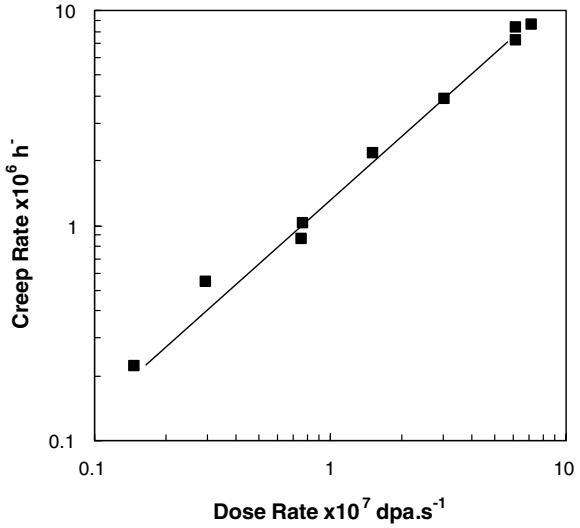

Fig. 6.1.1. Creep rate as a function of damage rate for cold-worked Zircaloy-2 pressure tube material irradiated with 4 MeV protons, from Ref. [72].

6.2. Effect of fast neutron fluence

Typically, if diametral strain is plotted against time or fast neutron fluence for a pressure tube irradiated at fast neutron fluxes typical of power reactors ($\sim 2 \times 10^{17}$ n m^{-2} s^{-1}, $E > 1$ MeV) with an internal pressure, there is a small positive intercept at the abscissa, Fig. 6.2.1 [15,25], suggesting a transient or primary creep strain. The transverse irradiation growth strain is negative and exhibits only a small transient over the first 1×10^{25} n/m^2, $E > 1$ MeV [56], Fig. 5.1.1, so this transient must be attributed mainly to creep. A similar transient is also observed at the edge of the reactor core where the irradiation creep is negligible [25]. Pressurized 'micro-pressure tube' specimens irradiated at very high flux ($\sim 2 \times 10^{18}$ n m^{-2} s^{-1}, $E > 1$ MeV) do not exhibit this intercept [17], presumably because the irradiation creep strain is relatively much larger, and hence this initial transient is likely attributable to thermal creep.

We have recently shown, however, that over the long term (16×10^{25} n/m^2, $E > 1$ MeV) the creep rate can vary slowly [30], as shown for example in Fig. 6.2.2. The change in strain rate may be positive or negative and its sign and magnitude depend upon temperature, stress and direction and probably relates to long term evolution of the microstructure, see Section 9.

6.3. Effect of temperature

From uniaxial in-reactor creep tests at high temperature (>600 K), stress relaxation tests at low and intermediate

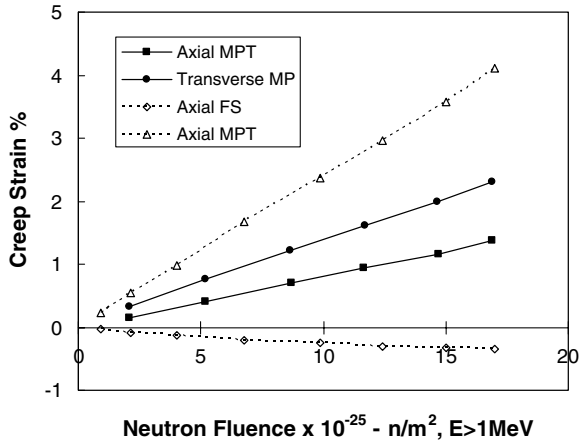

Fig. 6.2.1. Creep strain (total strain minus growth strain) as a function of neutron fluence for small pressurized tubes (Section 5.5) irradiated at 553 K in Osiris with a nominal stress of 160 MPa at a neutron flux of $\sim 2 \times 10^{18}$ n m^{-2} s^{-1}, $E > 1$ MeV, from Ref. [17].

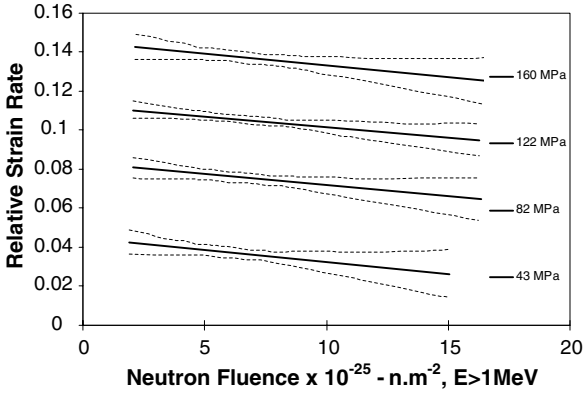

Fig. 6.2.2. Variation in 'steady state' creep rate with neutron fluence for small pressurized tubes irradiated at 553 K in Osiris at $\sim 2 \times 10^{18}$ n m^{-2} s^{-1}, $E > 1$ MeV, from Ref. [30].

temperature (310–570 K) and from the asymmetry of the diametral strain profiles caused by the coolant temperature changes in pressure tubes, we have previously inferred a general temperature dependence of the in-reactor creep rate. This is flat at low temperatures with a transition in the operating temperature range of pressure tubes in power reactors (520–580 K) to a relatively steep temperature dependence at higher temperatures ($\geqslant$600 K) [15], Fig. 6.3.1. In the high temperature range the temperature dependence can be expressed approximately by [14]

$$\dot{\varepsilon}_{\text{total}} \propto \exp(-T_{\text{act}}/T), \tag{6.3.1}$$

where $\dot{\varepsilon}$ is the strain rate, T the absolute temperature and T_{act} is the 'activation temperature' and has a value of around 17 000 K. This is about the value for thermal creep in this temperature range, variously reported as 15 000–25 000 K [73]. Possibly in-reactor creep is entirely thermal at these temperatures.

In the low to intermediate temperature range (310–580 K) we have inferred a temperature dependence of irradiation creep given by [74]

$$\dot{\varepsilon}_{\text{ic}} \propto \exp(-T_{\text{act}}/T) + 5.5 \times 10^{-6}, \tag{6.3.2}$$

where T_{act} has a value of 6500 K.

For the temperature range 555 K to 588 K this expression predicts an increase in strain rate of 56%, very close to the variation of creep compliances later observed in the axial and transverse directions of pressurized capsules of cold-worked Zr–2.5Nb irradiated in a fast neutron flux of $\sim 2 \times 10^{18}$ n m^{-2} s^{-1}, $E > 1$ MeV, i.e., 53% and 49%, respectively [75], Table 6.3.1 and Fig. 6.3.2. As the temperature is reduced, Eq. (6.3.2) becomes flat at about 450 K.

6.4. Effect of stress

At pressure tube operating temperatures, the stress dependence of irradiation creep of pressure tube materials is approximately linear, for stresses up to about 200 MPa, i.e.,

$$\dot{\varepsilon}_{\text{ic}} \propto \sigma^{n}, \tag{6.4.1}$$

where σ is stress and $n \sim 1$. The early evidence for this came from full size pressure tubes irradiated in the NRU Reactor at Chalk River Laboratories with zones of different stress created by machining to different wall thicknesses [76], Fig. 6.4.1. These tests typically ran for a relatively short time, typically 10 000 h at fluxes of about 2×10^{17} n m^{-2} s^{-1}, $E > 1$ MeV, or a fast fluence of $\sim 1 \times 10^{25}$ n m^{-2}, $E > 1$ MeV. Hence the contribution of growth was small compared to the total strain (see Fig. 5.1.1), and was not detected. Subsequently, stress relaxation of bent beams [77,78] supported the observation of linear stress depen-

Table 6.3.1
Creep compliances as a function of temperature for micro-pressure tube specimens irradiated in Osiris at 2×10^{18} n m^{-2} s^{-1}, $E > 1$ MeV

Temperature (K)	Axial creep compliance (m^2 n^{-1} MPa^{-1})	Transverse creep compliance (m^2 n^{-1} MPa^{-1})
555	0.55×10^{-30}	0.88×10^{-30}
588	0.84×10^{-30}	1.16×10^{-30}

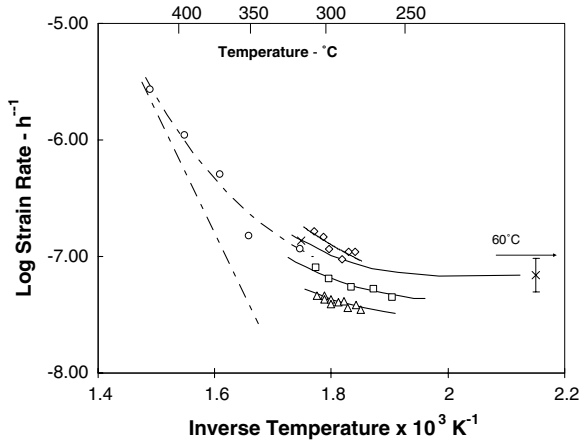

Fig. 6.3.1. Temperature dependence of the transverse strain rate of cold-worked Zr–2.5Nb pressure tubes and pressure tube material, from Ref. [15].

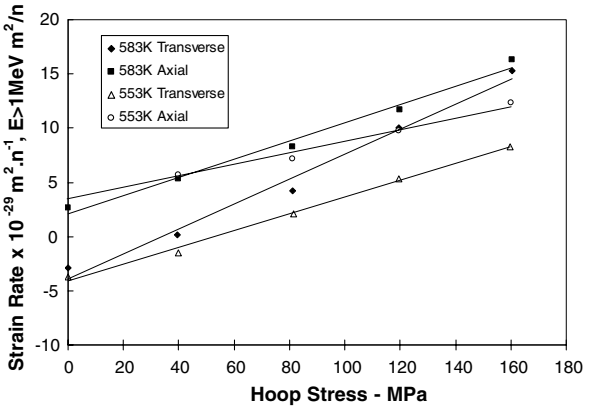

Fig. 6.3.2. Variation of strain rate in the transverse and axial directions with stress for Zr–2.5Nb micro-pressure tube material irradiated at 553 K and 583 K in Osiris at $\sim 2 \times 10^{18}$ n m^{-2} s^{-1}, $E > 1$ MeV, from Ref. [75].

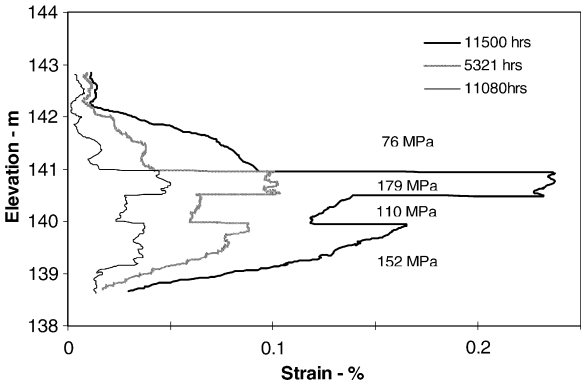

Fig. 6.4.1. Variation in accumulated strain with elevation for a Zr–2.5Nb pressure tube in the core of NRU. The wall thickness is varied to give the stress indicated and the peak neutron flux is $\sim 2\times10^{17}$ n m^{-2} s^{-1}, $E>1$ MeV, from Ref. [76].

dence. After a small transient the logarithm of stress decayed linearly with fast fluence or time indicating linear stress dependence of both the axial and diametral creep rates, Fig. 6.4.2.

Tests on pressurized capsules irradiated to very high fast fluences (1.6×10^{26} n m^{-2}, $E>1$ MeV) continue to show that irradiation creep varies approximately linearly with stress to at least 160 MPa [75], Fig. 6.3.2. In this case growth in the unloaded condition is obvious at the origin of the strain rate vs stress plot.

At stresses above 200 MPa, the stress sensitivity increases as shown graphically in Fig. 6.4.3 which is based on stress relaxation and uniaxial creep tests [79]. The latter include growth, but its contribution is small (typically $<2\times10^{-8}$ h^{-1} at the fluxes used to obtain the data) relative to the creep rates at the higher stresses ($\gg10^{-7}$ h^{-1}).

At temperatures above about 600 K, the stress sensitivity also increases gradually, based on tests on full sized pressure tubes in the WR1 reactor at Whiteshell Laboratories [14,15,80], Fig. 6.4.4. In these tests the ratio of transverse to axial stress (roughly 2:1 for a thin walled, closed

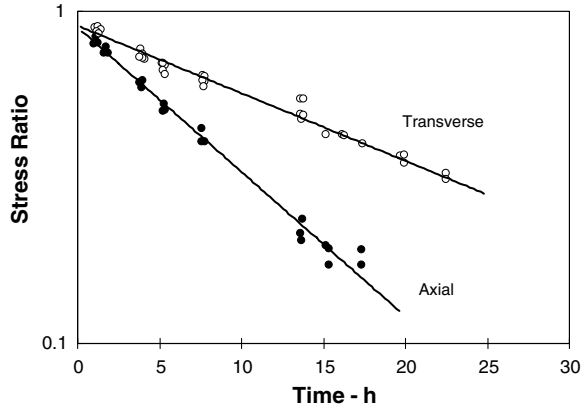

Fig. 6.4.2. Stress relaxation of bent beams of cold-worked Zr–2.5NB pressure tube material at $\sim2\times10^{17}$ n m^{-2} s^{-1}, $E>1$ MeV, in NRU at 573 K, from Ref. [77].

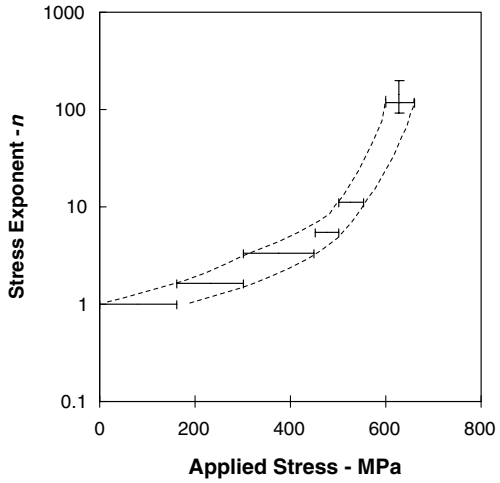

Fig. 6.4.3. Stress exponent of in-reactor creep of cold-worked Zr–2.5Nb pressure tube material as a function of applied stress, from Ref. [79].

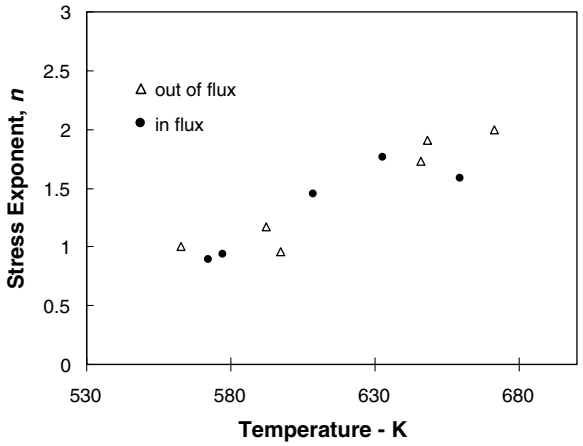

Fig. 6.4.4. Stress exponent as a function of temperature for cold-worked Zr–2.5Nb pressure tubes irradiated in the WR1 reactor. Data for sections of tubes both in and out of flux, from Ref. [15].

end pressurized tube) was often less than 2:1 because the pressurizing medium was an organic coolant, exhibiting a relatively high pressure drop relative to the average pressure as it flowed through the tube. In WR1, similar stress sensitivities were observed in both the fueled sections of the tubes (in-flux) and the pressure tubes extensions that passed through the shielding of the reactor (thermal creep only).

6.5. Effect of crystallographic texture

Before any observations were available, it was expected, based on the hcp crystal structure of zirconium, that irradiation creep would be anisotropic and that this anisotropy would be controlled by the crystallographic texture [81]. Uniaxial in-reactor creep tests and stress relaxation tests subsequently showed the expected higher creep rates in the axial than in the transverse direction of pressure tube

materials, Fig. 6.4.2 [76,77]. Holt and Ibrahim [51,67,74] developed a methodology for separating irradiation creep and growth in pressure tube deformation based on calculations of the expected anisotropy from the texture and on the elongation and diametral strain rates of pressure tubes in power reactors. This showed that creep made a substantial contribution to the elongation of pressure tubes and that growth reduced the diametral strain rate. We now know that about 33% of the elongation rate is due to irradiation growth and 67% due to irradiation creep while the contribution to diametral strain rate of creep is reduced about 25% by growth [61].

The effect of texture on the biaxial deformation behaviour has since been clearly demonstrated in tests on internally pressurized tubes of two different textures [17,52,75]. Some results are shown in Fig. 6.2.1. Here the irradiation growth has been subtracted from the total strain rate and only the irradiation creep is shown. The corresponding pole figures are shown in Fig. 5.5.1 and the texture parameters are given in Table 5.5.1.

Here it is clear that a material with a strong transverse texture, similar to that of a pressure tube, exhibits a relatively low transverse creep rate and a high axial creep rate, whereas a material with a more radial texture exhibits a relatively high transverse creep rate and a small negative axial creep rate. Note that the axial component of texture is small in both cases, and the axial creep rate depends upon the distribution of basal plane normals in the radial/transverse plane. Factors other than texture are believed to influence the anisotropy however, in particular a correlation of the dislocation substructure with crystal orientation [12,66] and possibly the interaction of the hcp α-phase with the bcc β-phase [82].

6.6. Effect of dislocation density

Causey et al. [77,83] showed, using stress relaxation tests, that the irradiation creep rate is weakly sensitive to the initial (as-manufactured) dislocation density, i.e., $\dot{\varepsilon}_{ic} \propto \rho^p$, where ρ is the dislocation density and p has a value of ~0.23, Fig. 6.6.1. Within the experimental variations this is comparable to the value ($\rho \sim 0.16$) found for Zircaloy-2 pressure tubes by extraction of creep and growth components from elongation and diametral strain data [67]. Like the growth, the creep rate and anisotropy probably depend on the mixture of dislocation types and their distribution amongst the different crystal orientations as well as the overall density [66].

6.7. Effect of grain size

The effect of grain size (the thickness of the flattened, elongated α-grains in pressure tubes) on irradiation creep has not been clearly established. Causey et al. [77] showed a very weak grain size dependence of the in-reactor creep rate for a variety of Zr alloys over a very wide grain size range, the creep rate increasing with grain size by about

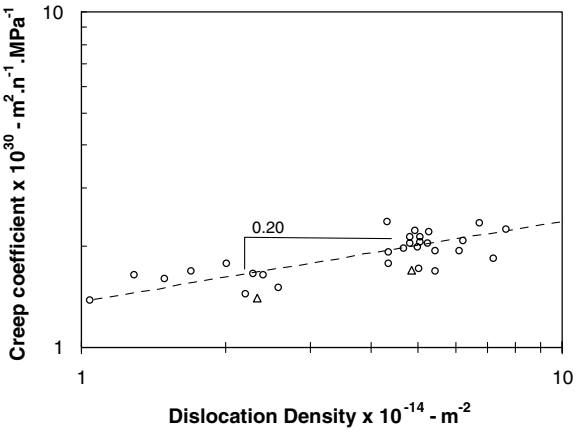

Fig. 6.6.1. Irradiation creep rate measured by stress relaxation as a function of pre-irradiation dislocation density. Irradiation in NRU at $\sim 2 \times 10^{17}$ n m^{-2} s^{-1}, $E > 1$ MeV and 573 K, from Ref. [83].

50% over a grain size range of 0.3–70 μm, but there are many potentially compounding factors. There are no studies in which the creep rate has been measured as a function of grain size alone. The creep rate has been shown, however, to increase from front to back of pressure tubes, coinciding with a reduction of grain size from about 0.4 to 0.3 μm and also with an increase in dislocation density and less transverse texture [22], see Section 3. Also the diametral strain rate of pressure tubes increases with decreasing grain size, Fig. 4.3, an observation which might also be attributed to a decrease in the absolute irradiation growth rate in that direction [54].

7. Thermal creep

Thermal creep contributes little to the peak diametral strain of a pressure tube or to elongation [14]. However thermal creep contributes the majority of the deformation at the ends of the channel where the fast neutron flux is low, but the bending moment in the pressure tube is high. It may thus contribute significantly to controlling the sag profile of the pressure tube and the potential for pressure tube-to-calandria tube contact. Also thermal creep may contribute significantly to the strain at high stresses, for example in the vicinity of a crack tip, and hence assist the relaxation of stresses that can potentially cause failure by the process of delayed hydride cracking [84,85].

The thermal creep of Zr alloys at about 570 K is complicated by the existence of strain aging [26,27], which can produce transient increases in strain rate during steady state creep and anomalous stress sensitivity in certain temperature and strain rate ranges. Strain aging in Zr is believed to be associated with solute effects.

7.1. Thermal creep at flaws

The stress concentrations at flaw tips in pressure tubes can initiate delayed hydride cracking under certain

conditions of stress, temperature history and hydrogen isotope concentration. Often the flaws will be present for many operating hours before the conditions exist which could initiate cracking. In this situation the peak stress at the flaw tip can relax by creep. The creep rate is fastest at the tip of the flaw where the stress is highest because of the strong sensitivity of creep rate to stress [79]. In the early stages of relaxation where the stress is still high, thermal creep may contribute to this relaxation.

The thermal creep behaviour of pressure tube and pressure-tube like material at temperatures of 373–596 K and stresses of 150–500 MPa with a variety of loading conditions is reported by Christodoulou et al. [73]. They noted substantial specimen to specimen variability which they attributed to variations in microstructure in their materials. They found that the steady state creep rate over most of the temperature range was approximately proportional to the 4th power of stress and the rate exhibited an activation temperature of 10 600 K above about 470 K and 5000 K below about 400 K. Analysis of the interaction of the crystallographic texture with the stress state showed that the creep was anisotropic with the creep compliance being higher in the basal plane than in the **c** direction of the hcp crystal lattice. Pre-irradiation reduces the creep rate, but the form of the creep law remains the same and the information derived above has been used to develop a model for local relaxation of stresses by thermal creep of pre-irradiated material at flaws [23,24], (see Fig. 7.1.1).

7.2. Thermal creep at the pressure tube ends

Early irradiations of Zr–2.5Nb pressure tubes in the NRU Reactor at Chalk River Laboratories showed a minimum in the diametral strain rate at the edge of the fuelled zone where the fast neutron flux is low [15], Fig. 7.2.1, for example [25]. This minimum was interpreted to represent the suppression of thermal creep by radiation damage accumulated at a neutron flux too low to induce significant irradiation creep. Because the estimates of flux in these locations were inaccurate, the quantitative interpretation of the shape of this profile in relation to the fast flux was not possible. Christodoulou et al. [14] interpreted this minimum as corresponding to in-reactor thermal creep, $\dot{\varepsilon}_{tc}$, of Eq. (2.1). A method of retrospective estimation of fast neutron fluence using ^{93}Nb was reported in 1990 [86], and results from such estimates were recently used to make a quantitative assessment of these strain profiles [25].

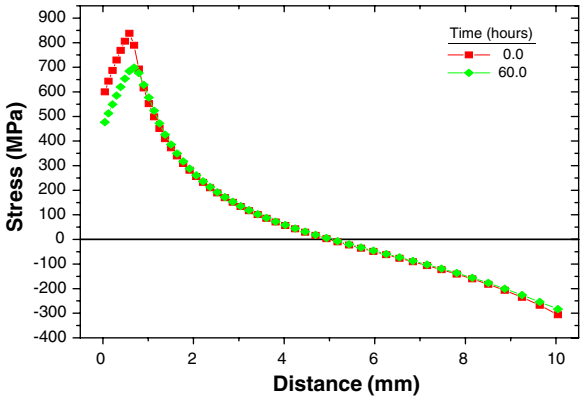

Fig. 7.1.1. Finite element calculation showing the relaxation of peak stress at a flaw in cold-worked Zr–2.5Nb pressure tube material after 60 h at 573 K, from Ref. [23].

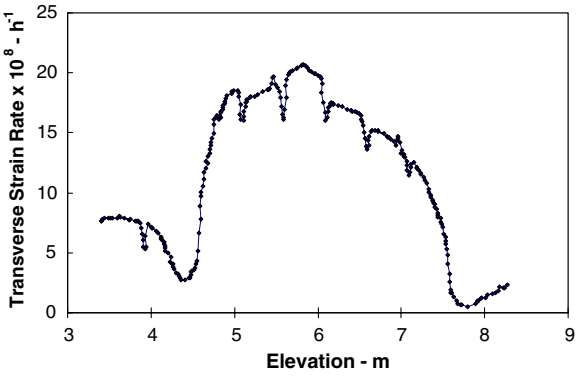

Fig. 7.2.1. Diametral strain rate as a function of elevation in NRU at 550–580 K with a peak neutron flux of $\sim 3 \times 10^{17}$ n m^{-2} s^{-1}, $E > 1$ MeV showing suppression of thermal creep at the edges of the core (4.4 m and 7.7 m), from Ref. [25].

The analysis shows that there is hardening that suppresses the thermal creep at fluxes lower than about 5×10^{15} n m^{-2}, $E >$ MeV. This is below the threshold fast flux for the formation of dislocation loop, $\sim 2 \times 10^{16}$ n m^{-2}, $E >$ MeV, and is attributed to immobilization by climb of dislocations that enable thermal creep. There is a further stage of hardening, in this case suppression of the irradiation creep above $\sim 2 \times 10^{16}$ n m^{-2}, $E >$ MeV, by the formation of dislocation loops that either inhibit glide or alter the distribution of self-interstitial atoms and vacancies at various 'sinks' or features in the microstructure. This distribution of point defects amongst various sinks is believed to be the basic mechanism of irradiation creep, see Section 10.

Making use of this information to improve the calculation of sag and potential contact is still some time off, however, because there appears to be a complicated interaction between temperature, flux, fluence and microstructure, and the stress dependence and anisotropy in this region are not well defined. This is one of the important remaining unknowns in the area of pressure tube deformation.

8. Creep ductility

The statement by Ells et al. [31] that 'an operating limit of 5% circumferential expansion seems to be very conservative' is based on the argument, first put forward by Woodford [87,88] that the total elongation of materials that fail in a ductile manner under tension is inversely related to the stress sensitivity of the strain rate (the inverse of the exponent n in Eq. (6.4.1)), Fig. 8.1. Superplastic materials

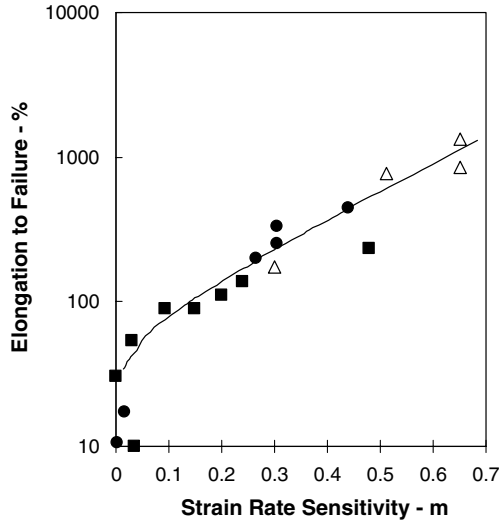

Fig. 8.1. Total elongation to failure in a tensile test as a function of strain rate sensitivity, $m = 1/n$, showing superplastic behaviour for $m > 0.5$, from Refs. [87,88].

generally have values of n in the range 1–2. For zirconium alloys in-reactor, $n \sim 1$ for stresses up to about 200 MPa, then n gradually increases, see Section 5.4. Under normal reactor operating conditions, at stresses of 100–150 MPa, it takes tens of years to reach strains approaching 5%, so in order to investigate that the limits of creep ductility in any practical time scale, it is necessary to do some form of accelerated test. The simplest way of doing this is to increase the stress, and hence the stress exponent, and thus such tests are thought to be naturally conservative. Ells et al. [31] summarized the data for cold-worked Zircaloy-2 and Zr–2.5Nb, in biaxial and uniaxial tests at stresses >300 MPa, where n has a value >5, Fig 8.2. The minimum failure ductility observed was 5.9%. Their conclusion

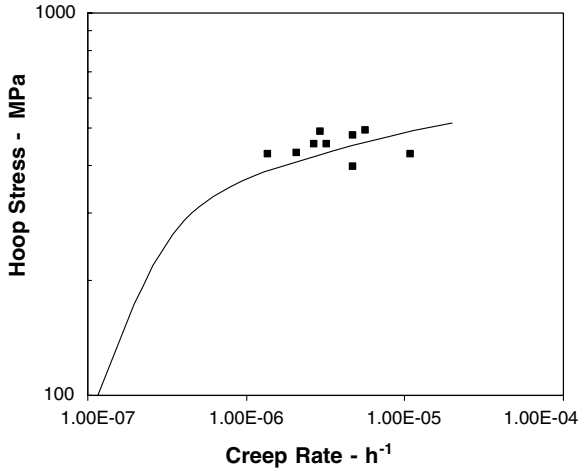

Fig. 8.2. Stress sensitivity of cold-worked Zr–2.5Nb pressure tube material, in-reactor varies from 1 (at <200 MPa) to 10 (at 300–500 MPa). The tests shown exhibited creep ductility of at least 5.9% and up to 17.2%, from Ref. [31].

quoted above is based on the fact that these tests are likely to be very conservative. One might debate this conclusion:

- The assumed failure mechanism is ductile necking. The relationship between ductility and stress sensitivity is not valid if some other failure mechanism intervenes. Irradiation creep in the low stress range involves the redistribution of material by the formation and migration to sinks of SIAs and vacancies. Over the course of a reactor lifetime each atom in a pressure tube is displaced form its position and rearranged 30–50 times to sinks such as dislocations on boundaries. The combination of elongation and diametral creep at ends of life represents an atomic rearrangement by radiation-induced mass transport approaching 10%. Hence microstructural and microchemical changes occur which are not experienced over the time scale of the accelerated tests and there is a possibility of an as-yet unidentified failure mechanism.
- The biaxial tests cited were done on fuel cladding, which has a predominantly radial texture [89]. This resists wall thinning under biaxial conditions and, as in the case of short term burst tests [90], and thus would be expected to impart increased ductility compared with the predominantly transverse texture of pressure tubes.

It should be noted that the safety analysis of a CANDU reactor assumes the possibility of a pressure tube rupture, and the system is able to tolerate this possibility without risk to the workers or the public.

9. Changes in microstructure and microchemistry during service

The changes that occur in the microstructure of pressure tube materials due to exposure to fast neutron flux and temperature during service have been documented by Griffiths and co-workers [12,22,91–93].

The most readily observable change is the appearance of **a**-type dislocation loops (Burgers vector $= 1/3(11\bar{2}0)$) a few tens of nanometers in diameter in the α-grains, Fig. 9.1. The number density of these increases rapidly in the first 1×10^{25} n m^{-2}, $E > 1$ MeV (roughly one year of operation), from the level present initially, then tends towards saturation, Fig. 9.2. The saturation level is a function of temperature and fast flux, increasing with fast flux and decreasing with temperature, so the profiles are expected to vary from channel to channel and reactor to reactor [93].

Coincident with this change is a slow increase in the **c**-component dislocation density over longer periods which depends upon crystal orientation [22]. Crystals with their **c**-axis in the radial direction of the tube initially contain mostly $1/3(11\bar{2}3)$ screw dislocations (approximately normal to the basal plane), and their dislocation density increases continuously with fast fluence, Fig. 9.2, by helical climb, as illustrated in Fig. 9.3. Crystals with their **c**-axis in

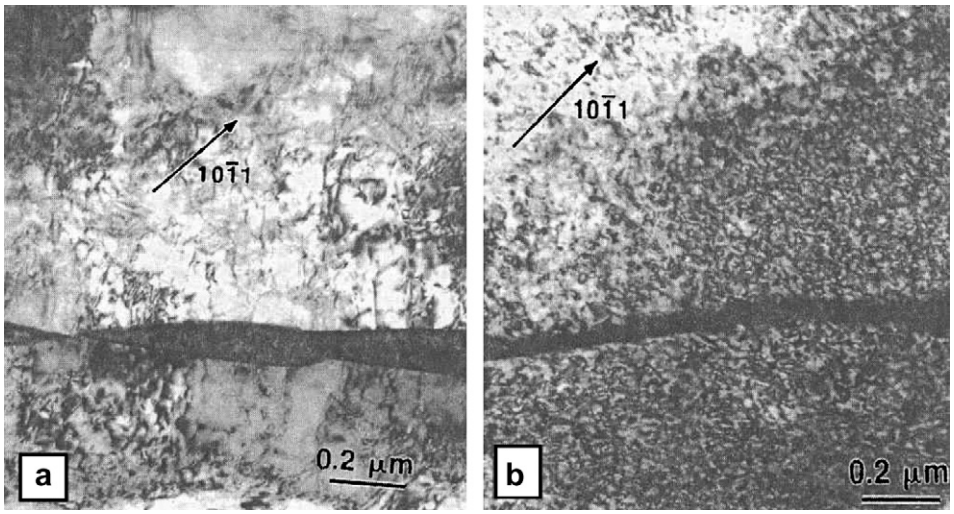

Fig. 9.1. Electron micrographs showing the **a** dislocation structure of Zr–2.5Nb pressure tube material, (a) before and (b) after irradiation at 543 K to a neutron fluence of 1.1×10^{26} n m^{-2}, $E > 1$ MeV. Note the high density of loops in (b), from Ref. [12].

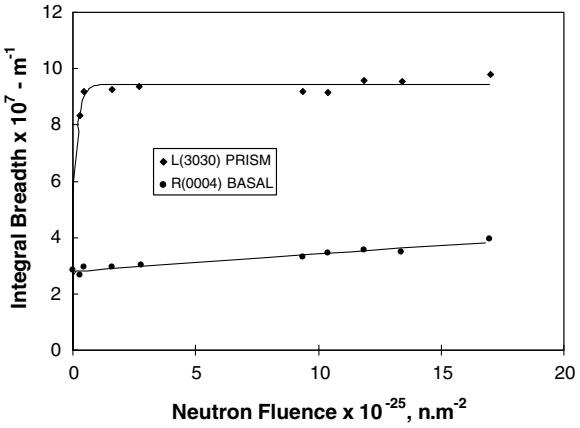

Fig. 9.2. Change X-ray line broadening due to **a**- and **c**-type dislocations density with neutron fluence at 543 K and $\sim 2 \times 10^{18}$ n m^{-2} s^{-1}, $E > 1$ MeV, from Ref. [12].

the transverse direction contain mainly $1/3(11\bar{2}3)$ edge dislocations (approximately parallel to the basal plane). Initially these tend to split into two partials $1/\bar{6}(20\bar{2}3)$, causing an initial apparent reduction (based on X-ray line broadening) but also actually reflecting some increase in the **c**-component dislocation density.

After a fluence of few $\times 10^{25}$ n m^{-2}, $E > 1$ MeV, the Nb in the α-phase, which is slightly super-saturated before irradiation, precipitates as fine Nb rich particles 2–5 nm in diameter, Fig. 9.4, which are uniformly dispersed, except near the grain boundaries where a narrow region is denuded [92]. There is an indication that the concentration of Nb in the matrix is reduced to an estimated 0.3%.

The state of β-phase, which before irradiation has partially transformed towards equilibrium and contains ~50%Nb, tends towards a steady state after irradiation to about 2×10^{25} n m^{-2}, $E > 1$ MeV, Fig. 9.5. The steady

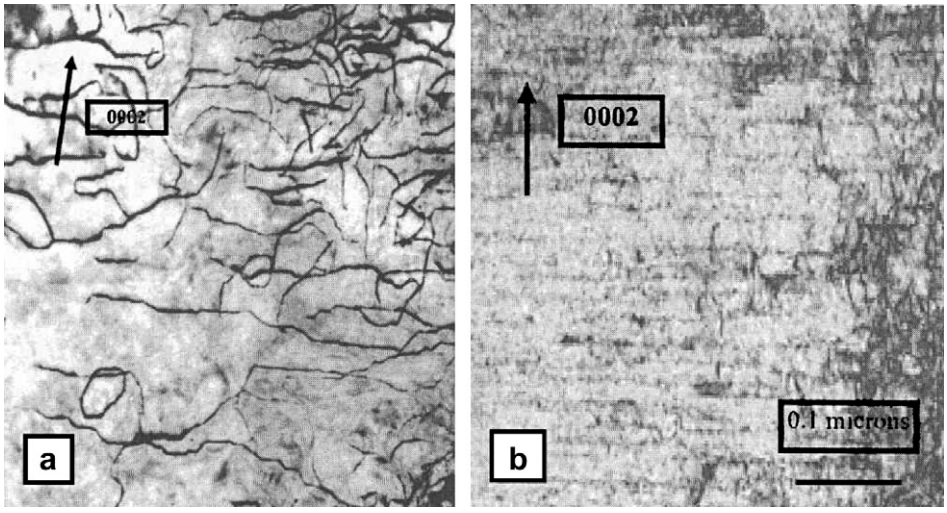

Fig. 9.3. Electron micrographs showing the **c**-type dislocation structure of Zr–2.5Nb pressure tube material, (a) before and (b) after irradiation at 543 K to a neutron fluence of 1.1×10^{26} n m^{-2}, $E > 1$ MeV. Note loop nucleated on a screw dislocation at arrow in (b), from Ref. [12].

state condition depends upon temperature and fast flux [93]. At the high flux region towards the inlet end and in the middle of the core, the transformation towards equilibrium is reversed and the β has about 40%Nb. At the inlet end there is a very slow progression towards the equilibrium state and at the outlet end this progression is more rapid. Fig. 9.6 shows a compilation of data for fluences of $>2\times10^{25}$ n m^{-2}, $E>1$ MeV.

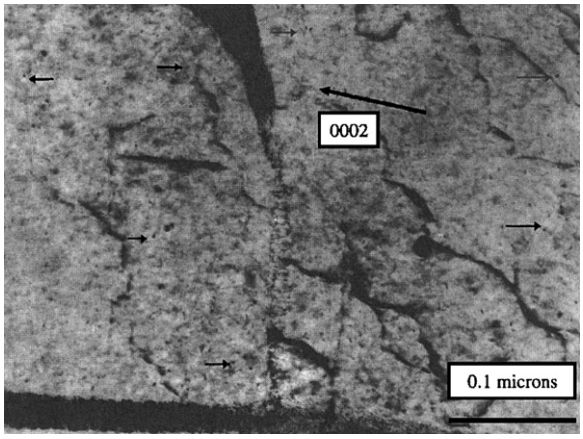

Fig. 9.4. Electron micrograph showing Nb precipitates (arrows) in the α-phase of Zr–2.5Nb pressure tube after irradiation at 573 K to a neutron fluence of 0.9×10^{25} n m^{-2}, $E>1$ MeV, from Ref. [92].

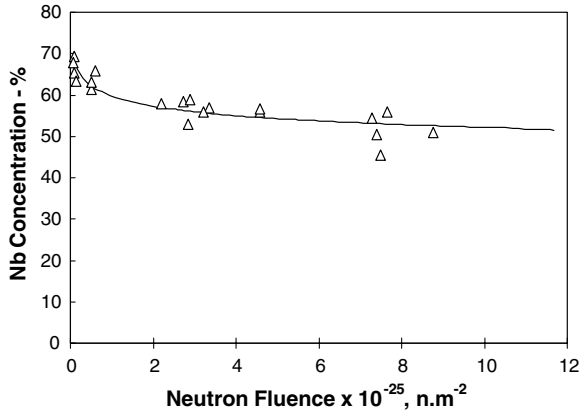

Fig. 9.5. Variation in the Nb concentration in the β-phase with neutron fluence in a CANDU pressure tube operating at ~560–570 K, with a peak flux of $\sim3\times10^{17}$ n m^{-2} s^{-1}, $E>1$ MeV, from Ref. [92].

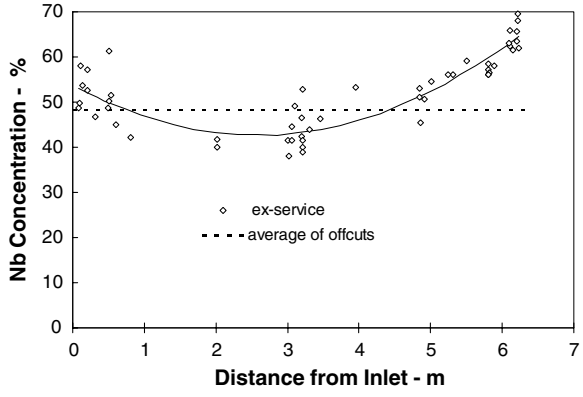

Fig. 9.6. Variation in the Nb concentration in the β-phase along a CANDU pressure tube operating at ~520–570 K (inlet to outlet) with a peak neutron flux of $\sim3\times10^{17}$ n m^{-2} s^{-1}, $E>1$ MeV, from Ref. [92].

The Fe which is initially concentrated in the β-phase is dispersed by irradiation and can no longer be detected within the β or in the α-grains because its average concentration is below the limit of detection (~0.15%) [44]. Fe is still found at the α–α sub-boundaries however at approximately the same level as before irradiation.

10. Mechanisms of irradiation-induced deformation

This section will strictly deal with the deformation mechanisms associated with irradiation. Thermal creep is a vast subject about which many textbooks have been written, however, its contribution to in-reactor deformation of pressure tubes is small once irradiation hardening has occurred. For an overview of thermal creep in Zr alloys, see the article by Harbottle [26] and for a more detailed account see the book by Franklin et al. [27].

The effects of irradiation on dimensional stability are generally acknowledged to be due to 'displacement damage' that is the knocking of atoms off their lattice sites by momentum transfer from the radiation. In pressure tubes the vast majority of displacement damage comes from the fast neutrons. The damage occurs in 'displacement cascades'. Once an energetic neutron has displaced one Zr atom, sufficient energy is usually transferred that the zirconium atom (which interacts very much more strongly with the other Zr atoms that the initial neutron) displaces many more atoms. The residual damage after a very short (ns) period during which the kinetic energy of the displaced atoms is dissipated, comprises vacant lattice sites (vacancies), Zr atoms in interstitial sites (self-interstitial atoms or SIAs) and clusters of two or more of each of these defects. The point defects (vacancies and SIAs) which may represent only a few per cent of the total number of atoms displaced, are mobile at reactor operating temperatures, and the dimensional changes caused by creep and growth are related to the disposition of these defects [94]. At higher temperatures (>700 K) where significant numbers of vacancies are formed thermally and at lower temperatures (<400 K) where the vacancies are immobile, the clusters are believed to play an important role [95,96].

10.1. Irradiation growth

In the temperature range at which power reactors operate, the SIAs and vacancies can be annihilated in two ways: by reaction with a defect of the opposite sign either singly or in a cluster, or reaction with an extended lattice defect or 'sink' (dislocation, loop, phase- or grain-boundary). In the former case no strain occurs. In the latter case a strain occurs locally in a direction characteristic of the defect. In the case of a dislocation or loop the strain is a contraction

(for vacancies) and a dilation (for SIAs) in the direction of the Burgers vector. In the case of a boundary it is a contraction or dilation in the direction of the boundary normal.

Two conditions are necessary for a macroscopic strain to occur from the disposition of point defects at sinks. First, the sinks must experience 'net' fluxes of point defects, i.e., the flux of one species of point defect must, over time exceed the flux of the species of the opposite sign. Obviously, if a particular sink experiences at net flux of one species, some other sink must experience a net flux of the other species. Second, the orientation distribution of the sinks that experience net fluxes of the different species of point defect must be different.

The factor which determines the net flux of a particular point defect to a particular sink is referred to as a 'bias' and is by definition negative for vacancies and positive for interstitials. Note that it is only necessary for one type of sink to have a bias. By default unbiased or 'neutral' sinks will experience a net flux of defects of the opposite sign. A number of sources of bias have been proposed for Zr alloys [54], but the commonly accepted one is diffusional anisotropy difference (DAD) first proposed by Woo and Goesele [97,98]. They proposed that vacancies and SIAs exhibit anisotropic diffusion in Zr – a natural consequence of the hcp crystal structure, and that the diffusional anisotropies of the two species of defects are different, a natural consequence of the different relationship of the two defects to the hcp lattice. This provides a very powerful driving force to segregate the defects amongst sinks of different orientation. Growth results when the strain direction of a sink correlates with its orientation.

For boundaries this is self-evident, since the strain direction is normal to the boundary. In the case of **a**-type and **c**-component network dislocations the orientation correlates with dislocation character so that **c**-component edge dislocations are effectively on the basal plane and **a**-type edge dislocations are effectively perpendicular to it. Since the point defects interact more strongly with and edge than a screw dislocation [99], this provides an orientation bias [54]. In the case of **a**-type loops the loop plane is normal to the basal plane as is some part of the line direction. Both the plane and line direction of **c**-component loops are on the basal plane. In a material containing only dislocation sinks (or coarse grained material), preferential diffusion of SIAs in the basal plane or vacancies normal to it will lead to the observed shrinkage along then **c**–axis and expansion in the basal plane. If a high density of boundaries are introduced (fine grained material) the growth can be a complex function of the dislocation densities and grain shapes. Qualitatively, the growth behaviour of the TG3 R1 material, i.e., simultaneous shrinkage in the axial and transverse direction of the pressure tube (see Section 5.6) is predicted for very fine grains [54,98], Figs. 10.1.1 and 10.1.2.

Detailed mathematical treatments of models for irradiation growth are given in Refs. [54,94–99].

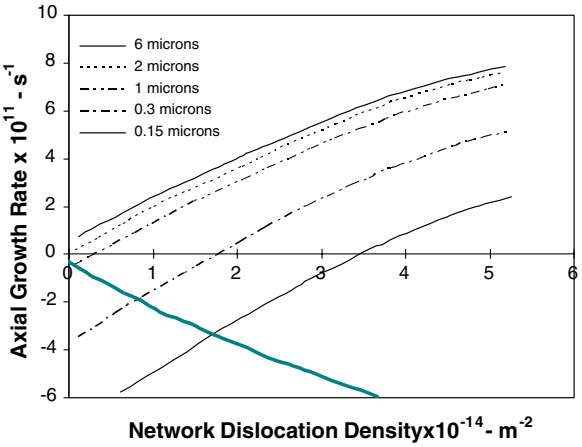

Fig. 10.1.1. Calculated effect of dislocation density and grain thickness of the growth rate of Zr–2.5Nb in the axial direction, from Ref. [54]. In the region between the heavy line and the *x*-axis both the axial and transverse growth rates are negative.

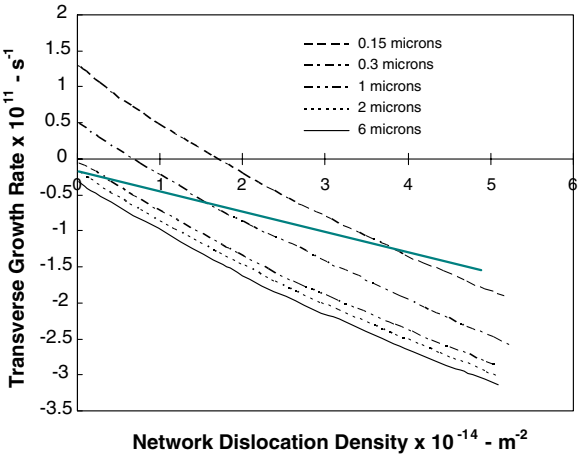

Fig. 10.1.2. Calculated effect of dislocation density and grain thickness of the growth rate of Zr–2.5Nb in the transverse direction, from Ref. [54]. In the region between the heavy line and the *x*-axis both the axial and transverse growth rates are negative.

10.2. Irradiation creep

Unlike growth, there is no consensus regarding the mechanisms of irradiation creep in Zr alloys, other than that it is related in some way to net fluxes of point defects to sinks, probably dislocations and loops.

Models for irradiation creep that have been considered for zirconium include yielding-creep, climb-plus-glide (CPG) including 'I-creep' and various forms of stress-induced preferred absorption (SIPA) including SIPA-DAD or elasto-diffusion (SIPA induced by the effect of stress on diffusional anisotropy). These models, amongst others, have been reviewed by Matthews and Finnis [100].

The yielding creep model [101,102] is applicable to materials exhibiting irradiation growth. According to this model the internal stresses generated by growth of individual grains of different orientations approach the yield stress,

and the applied stress elevates the stress in crystals of a certain orientation above the yield stress causing them to yield. Continued growth causes continued yielding in a direction that is biased by the applied stress. This model has generally been ignored in recent times, but has not been discounted by experimental facts.

The climb-plus-glide model [103] is an extension of the dislocation creep model [104] of thermal creep in which dislocations are able to bypass obstacles by climb due to the absorption of thermally generated vacancies. The strain producing step is glide. Under irradiation, a net flux of either vacancies or interstitials to a given dislocation will allow it to bypass obstacles and glide. In the late 1970s this model was supported by an experiment in which the neutron flux to a creeping specimen was turned on and off by moving the creep rig in and out of reactor [105]. A positive strain transient was seen in both cases, even though on initiating irradiation, the dislocations in the specimen would experience a net flux of SIAs corresponding to the build up of a vacancy super-saturation, while on terminating the irradiation a net flux of vacancies would be expected as the super-saturation decayed. This result has never been explained by another mechanism. A modification of this model is Gittis' I-creep model [106], in which there is coordinated movement of arrays of dislocations by glide after climb.

More recently Semenov and Woo [107] have developed an analysis of the stochastic nature of displacement cascade damage in both time and space, show that a net flux of point defects to dislocations may not even be necessary for them to surpass obstacles and glide, given that the fluctuations in the defect fluxes of the two species are large enough.

SIPA [106,108–110] assumes a bias of the flux of point defects to dislocations as a function of the orientation of the Burgers vector with respect to the applied stress. Dislocations whose Burgers vectors are aligned with the tensile stress experience a net flux of SIAs. By default, those aligned with a compressive stress experience a net flux of vacancies. Any deviatoric stress tensor will induce a bias.

This bias was initially attributed to the elastic interactions of the point defects with and the strain fields of the dislocations in a stress field [100]. The point defects are considered as inclusions with elastic properties different from the matrix. The key feature for SIPA to be viable is that the SIA must to exhibit an effective shear modulus less than that of the matrix while the vacancy exhibits a shear modulus similar to that of the matrix. This might not always be the case. Another possibility is that the dislocations are not perfect sinks (as is often assumed in calculations of creep and growth) but that there is a barrier to absorption. This barrier may then be a function of stress and different for interstitials and vacancies [100]. Finally there is the concept that the anisotropy of point defect migration is stress dependent [98], so the applied stress modifies the DAD effect. This is referred to as SIPA_DAD or elasto-diffusion (ED).

Detailed mathematical treatments of the models for creep are given in the Refs. [98–110].

11. Modelling pressure tube deformation

11.1. The need for models

Models are required to predict the deformation of modified pressure tubes operating in new reactor designs under conditions different from those that have been experienced previously or to predict the future deformation of pressure tubes in existing power reactors for the purposes of plant life management (PLiM).

In the case of new reactor designs the operating conditions, flux, temperature, coolant pressure, may be more severe so that the thickness of the tube must be adjusted. Also, one may want to take advantage of the knowledge of the effects on deformation of microstructural, chemical and manufacturing variables to improve the deformation behaviour in order to achieve a satisfactory pressure tube life in the new design. An example of such a new design is the 1000 MWe class Advanced CANDU Reactor (ACR 1000 [16]) which has higher coolant temperatures and pressures for improved thermodynamic efficiency, and higher channel powers for increased average power density of the core.

In the case of PLiM, a general algorithm for managing the life of the pressure tubes in a CANDU reactor is as follows [7]:

- plan maintenance based on predictions using models based on R&D and surveillance data;
- monitor on-going changes to verify predictions/modify models;
- disposition 'out-of-design' conditions, e.g., flaws and contact of PT with CT (this could involve removal of tubes);
- continued R&D including end-of-life testing to improve models;
- modify maintenance plans accordingly.

In many cases, it may be sufficient simply to extrapolate data from previous inspection campaigns, for example, the elongation of each pressure tube in a CANDU 6 reactor can be measured every time that the fuelling machine refuels that channel. Here a linear extrapolation of the data to the next maintenance outage may be sufficient, and for longer term planning it may be simply a matter of knowing how to extrapolate the data (e.g., a quadratic equation).

In other cases, there is no alternative but to use a model. This is the case for spacer location and repositioning (SLAR)[37], the objective is to prevent contact of the hot pressure tube with the cold calandria tube late in life when the deuterium concentration of the pressure tubes has increased to reach a critical level. In earlier CANDU reactors the spacers, helical springs circling the pressure tube to

centre it in the calandria tube, Fig. 1.1.1, were loose and were found to move during service [38]. This caused the rupture of a Zircaloy-2 pressure tube in the Pickering Unit 2 reactor in 1983 as a result of pressure tube sagging into contact with the calandria tube and the formation of zirconium hydride blisters on the outside of the pressure tube at the line of contact [29].

At that time, there were 20 reactors constructed or in-service with the loose spacer design. Fortunately 18 of these units had Zr–2.5Nb pressure tubes which exhibit a much lower deuterium pick-up rate than Zircaloy-2. The two reactors with Zircaloy-2 tubes were immediately shut down for retubing, the spacers for new reactors were changed to a tight-fitting design [38], and a maintenance procedure called SLAR was developed for the 18 reactors with loose spacers and Zr–2.5Nb tubes.

The response of the horizontal pressure tube-calandria tube assembly to the weight of the fuel and coolant is an elastic deflection several millimeter as a result of the bending moment. During operation a permanent sag is developed due to irradiation creep of both the calandria tube and the pressure tube a process referred to as 'creep-sag'. The annealed Zircaloy-2 calandria tube exhibits a much higher resistance to creep-sag than the pressure tube so in the first few years of operation the pressure tube sags to transfer most of the load of fuel and coolant to the calandria tube through the spacers [18]. Thereafter the gross sag of the assembly is controlled by the calandria tube and the pressure tube properties determine the rate at which the pressure tube approaches contact with the calandria tube between the spacers [19]. If the spacers are displaced, this may happen before the end of the design life and there is a potential for blister formation.

In the SLAR process, an instrumented tool is inserted into each pressure tube which can detect the spacers, apply an upward bending moment to the inside of the tube to 'lift' it so that the spacers are free to move and apply an electromagnetic pulse to move the spacers with a linear induction motor [37]. This process has proven very successful at all the reactors with the loose spacer design. The question arises, 'Where should the SLAR operator leave the spacers?' Since the pressure tube and calandria tube have already undergone plastic deformation, each assembly is now unique. A deformation model is used to answer the question [19,20].

The model comprises three elements, a two dimensional finite element representation of the fuel channel, CDEPTH [19], a calandria tube deformation equation and a pressure tube deformation equation. The deformation equation for the pressure tube must predict its response to bending moments – essentially a uniaxial loading in the axial direction of the tube. Because the calandria tube controls the gross sag (which *can* be easily measured) there is no reactor measurement of this response. A model is required to predict this response, based upon the measurable deformation responses of the pressure tube to a biaxial stress state, i.e., elongation and diametral strain. The most important aspect of such a model is the dependence of the anisotropic deformation behaviour on the multi-axial stress tensor.

11.2. Models for anisotropic creep and growth

To describe the deformation behaviour of pressure tubes under a multi-axial stress state, an 'anisotropic deformation equation' is required for anisotropic creep and growth of the material. Combined with an equivalent equation for the calandria tube, such an equation can then be used as input to a finite element model to predict the deformation of the fuel channel, and in particular the sag and the potential for pressure tube-to-calandria tube contact. The simplest anisotropic formulation for creep is that derived by Ross-Ross et al. [76] from Hill [111]. Such an equation contains three independent anisotropy parameters, and thus requires the measurement of three independent deformation rates under at least two different stress states. The parameters for such a model cannot, therefore, be derived solely from the elongation and diametral strain data from a pressure tube. Because the stress exponent $n \sim 1$ in Eq. (6.4.1), the expressions derived by Ross-Ross et al. are consistent with the 'polycrystalline' approaches described below. However, the polycrystalline models allow assumptions about the deformation mechanisms to be substituted for measurements.

The first anisotropic deformation model for pressure tubes [75] did not separate irradiation growth, which had not yet been observed, from the total deformation rate which was treated entirely as creep. The first deformation equations separating creep and growth were developed in the late 1970s [51,67,74]. The anisotropic effects of texture were taken into account by averaging the behaviour of individual crystals, assuming certain strain-producing mechanisms at the single crystal level in what is referred to as a 'polycrystalline model'. This was a 'lower bound' polycrystalline model, which ignores the fact that different orientations of crystals have different strain tensors. The anisotropy of the polycrystal (the pressure tube) depends upon the relative contributions of the strain mechanisms at the single crystal level. This was derived from bent beam uniaxial stress relaxation tests in which the growth component does not contribute to the measured strain [77–79,83,112] and allowed the prediction of the creep anisotropy of a pressure tube under biaxial loading. The growth anisotropy was derived again using a lower bound polycrystalline model, by assuming, that at the single crystal level, dislocations were the sinks for SIAs, and grain boundaries were the sinks for vacancies. Once the anisotropy of creep and growth were defined, their contributions to elongation and diametral strain in a given power reactor could be derived from the elongation and diametral strain data for that reactor, and the response of a pressure tube to a multi-axial stress state, including sag [113], could be predicted.

In the mid 1980s, an 'upper bound' approach was used (in which all crystals are assumed to exhibit the same strain

tensor) to study the effects of interactions between the crystals [68,69]. The approach was developed mainly to explain the irradiation growth response of calandria tube materials [35,69]. The parameters of the model were derived by the same methodology as those for the earlier lower bound model, but including data for creep in shear as well as stress relaxation [83]. At the same time finite element methods were used to calculate the sag more accurately [19,114].

Both the upper and lower bound approaches can lead to systematic errors in predictions for stress tensors different from those for which the data are obtained to normalize the model. As concerns about the accuracy of sag predictions for the SLAR application developed in the early 1990s (see previous section), a 'self-consistent' polycrystalline model, SELFPOLY, was developed which allowed for individual crystals to deform differently, but under constraints imposed by the surrounding matrix of crystals with different orientations [115]. The single crystal creep and growth are deconvoluted from in-reactor data for polycrystalline pressure-tube and pressure-tube like materials tested with a range of stress tensors including uniaxial tension, biaxial tension and shear [116,117]. The single crystal growth parameters could for the first time be based on growth data coming from tests in high flux reactors [12,61].

This model, currently in use, represents the behaviour of the tubes quite well over a narrow range of textures close to those of pressure tubes, but there are inconsistencies in the predicted creep anisotropy when the texture is changed significantly [118], Fig. 11.2.1. This is likely due to secondary contributing factors to the anisotropy, including anisotropic grain shape, anisotropic dislocation distributions introduced during manufacturing, and the presence of an isotropic second phase. A variation of the self-consistent polycrystalline model, applicable for the case when the stress exponent $n \neq 1$ in Eq. (6.4.1), SELFPOLY-N has also been developed [119] for the case of thermal creep near the ends of the pressure tube and for high stresses relevant to the relaxation of stresses at flaws [23,24].

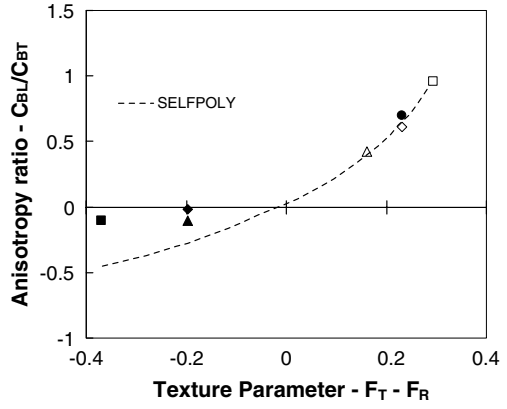

Fig. 11.2.1. Comparison of measured and calculated (from texture) anisotropy ratios (axial strain rate:transverse strain rate) for internally pressurized tubes under irradiation creep conditions, from Ref. [118]. The open square represents CANDU pressure tubes. F_T and F_R are defined in Section 3.

11.3. Model for pressure tube deformation

Although the means to predict polycrystalline behaviour from the behaviour of individual crystals now exist as described above, the basic physical parameters that would be needed to construct reliable mechanistic models to predict the deformation of even a pure Zr single crystal are not known (e.g., mobility and anisotropy, configuration, elastic properties of point defects, structures of dislocation cores, and the influence of impurity atoms on these characteristics). We therefore still rely a phenomenological approach.

The complex interaction between the effects of temperature and fast neutron flux on the deformation has led to the development of analyses that assume that long term steady state deformation consists of separable, additive components from thermal creep, irradiation creep and irradiation growth as given in Eq. (2.1) [14]. All three components are anisotropic and contribute to length as well as diameter changes. They are given by

$$\dot{\varepsilon}_d^{tc} = [K_1 C_1^d \sigma_1 + K_2 C_2^d \sigma_2^2] \exp(-Q_1/T) + K_3 C_1^d \sigma_1 \exp(-Q_3/T), \quad (11.3.1a)$$

$$\dot{\varepsilon}_d^{ic} = K_c K_4(x) C_4^d(x) \sigma(x) \phi [\exp(-Q_4/T) + K_5], \quad (11.3.1b)$$

$$\dot{\varepsilon}_d^{ig} = K_g K_6(x, \phi t) C_6^d(x) \phi \exp(-Q_6/T). \quad (11.3.1c)$$

The in-reactor thermal creep component has two terms [14] that dominate at temperatures above and below 570 K, respectively. The last two terms describe flux-dependent creep and irradiation growth, respectively. The stress exponent for thermal creep varies with stress: for stresses below 120 MPa, the stress exponent is 1, while for stresses between 120 and 200 MPa, the stress exponent increases to 2 [78]. The parameters in Eq. (11.3.1) are defined as follows:

- $\dot{\varepsilon}_d$ strain rate in a direction d (i.e., radial, transverse, axial), h^{-1};
- $\dot{\varepsilon}K_1, K_2$ constants for high temperature in-reactor thermal creep;
- K_3 constant for low temperature in-reactor thermal creep;
- $K_4(x)$ function describing the variation of irradiation creep due to variations of microstructure along the length of the tube;
- x distance from the back end of the tube;
- $K_6(x, \phi t)$ function describing the variation of irradiation growth due to variations of microstructure along the length of the tube as a function of fluence;
- C_1^d, C_2^d anisotropy factors due to texture for in-reactor thermal creep in a given direction d and for stress exponents, n, of 1 and 2, respectively;

$C_4^d(x), C_6^d(x)$ anisotropy factors due to texture for irradiation creep and growth, respectively, in a given direction d along the length of the tube;
K_c, K_g constants for irradiation creep and growth, respectively;
Q_1, Q_3, Q_4, Q_6, K_5 activation temperatures and constant, respectively;
σ_1, σ_2 effective stresses in MPa for thermal creep and stress exponents, n, of 1 and 2;
$\sigma(x)$ effective stress for irradiation creep, MPa;
T temperature, K;
ϕ fast flux, n/m^2/s ($E > 1$ MeV);
t irradiation time, s.

The equivalent stresses σ_1, σ_2 and $\sigma(x)$ are related to the radial, axial, and transverse stress σ_r, σ_a and σ_t, respectively, by means of the Hill's anisotropy coefficients [74,111], namely,

$$\sigma_i = [F_i(\sigma_a - \sigma_t)^2 + G_i(\sigma_t - \sigma_r)^2 + H_i(\sigma_r - \sigma_a)^2]^{1/2}. \tag{11.3.2}$$

The subscript i stands for 1 (i.e., $n = 1$), 2($n = 2$), or in the case of irradiation creep $\sigma_i = \sigma(x)$.

The values of the Hill's anisotropy coefficients for thermal creep, F_i, G_i and H_i ($i = 1, 2$) are average values calculated from the crystallographic textures of pressure tubes based on the non-linear polycrystalline model, SELFPOLY-N [119], assuming a combination of slip on prism, basal and pyramidal systems that is consistent with out-reactor biaxial, uniaxial and torsion creep tests on small tubes with textures and microstructure similar to pressure tubes. The dependencies of Hill's anisotropy constants for thermal creep on x were neglected because of the relatively small magnitude of the thermal component.

Once the anisotropy parameters for thermal creep have been established, the values of K_1, K_2 and Q_1 (~17 000 K) for high temperature thermal creep are derived from high temperature biaxial creep data from the WR1 Reactor and uniaxial creep data from NRU [15]. Similarly, the values of K_3 and Q_3 (~1000 K) are obtained from diametral strain data at the edge of the core of a pressure tube irradiated in NRU [14,25]. In both cases, the data reflect thermal creep of irradiation hardened materials.

The values of the Hill's anisotropy coefficients for irradiation creep, F_i, G_i and H_i, $i = 4$, are average values derived from the crystallographic textures of power reactor pressure tubes using the self-consistent polycrystalline model, SELFPOLY [115], based on single crystal creep compliances. The single crystal creep compliances are deconvoluted from in-reactor data as described in Section 10.2 [117].

The Hill's anisotropy constants for irradiation creep depend on the distance, x, from the back end of the tubes, and for a 6-m tube this dependence is given by

$$\begin{aligned} F(x) &= F^b + (F^f - F^b)x/6, \\ G(x) &= G^b + (G^f - G^b)x/6, \\ H(x) &= 1.5 - F(x) - G(x). \end{aligned} \tag{11.3.3}$$

Here F^b, F^f, G^b and G^f are the values of Hill's anisotropy constants F and G at the back and front ends of the tube.

Using the terminology employed in Eq. (11.3.2), the anisotropy factors due to texture for in-reactor thermal or irradiation creep are given by

$$\begin{aligned} C_i^r &= [H_i(\sigma_r - \sigma_a) - G_i(\sigma_t - \sigma_r)], \\ C_i^t &= [G_i(\sigma_t - \sigma_r) - F_i(\sigma_a - \sigma_t)], \\ C_i^a &= [F_i(\sigma_a - \sigma_t) - H_i(\sigma_r - \sigma_a)]. \end{aligned} \tag{11.3.4}$$

Here $i = 1$, 2, 4 or 6, and C is a function = nction of (x) when $i = 4$ or 6.

The coefficient describing the end-to-end effect of the rate of irradiation creep along the length of the tube is given by

$$K_4(x) = K_{4-1} + K_{4-2}x. \tag{11.3.5}$$

Here K_{4-1} and K_{4-2}, are constants derived from in-reactor stress relaxation tests from specimens taken from different positions relative to the back end of a tube.

The growth coefficient describing the end-to-end effect and the dependence of growth on fluence is given by

$$K_6(x, \phi t) = (K_{6-1} + K_{6-2}x)(1 + C/B[\phi t]). \tag{11.3.6}$$

Here K_{6-1} and K_{6-2} are constants derived from the average end-to-end variation in grain thickness and from a theoretical model for the effect of grain thickness on growth [54]. The growth anisotropy factors are given by

$$\begin{aligned} C_6^a(x) &= G_a^b + (G_a^f - G_a^b)x/6, \\ C_6^t(x) &= G_t^b + (G_t^f - G_t^b)x/6, \\ C_6^r(x) &= -C_6^a(x) - G_6^t(x). \end{aligned} \tag{11.3.7}$$

Here G_a^b, G_a^f, G_t^b and G_t^f are anisotropy parameters derived from polycrystalline irradiation growth data from OSIRIS [12,52]. The single crystal growth strain rate tensors are deconvoluted from the polycrystalline data using SELFPOLY and the single crystal creep compliance coefficients mentioned above. SELFPOLY is then used to calculate K_g, G_a^b, G_a^f, G_t^b and G_t^f. The temperature dependence of growth represented by Q (~−3000 K) is derived from the growth data from OSIRIS.

Once the growth and thermal creep parameters are established, the irradiation creep rates can be extracted from the power reactor data (in this case data from the pressure tubes in Pickering A were used to obtain biaxial data comprising only irradiation creep). Values of K_c, Q_4 (~9900 K) and K_5 (1.1×10^{-7}) could then be derived.

Fig. 11.3.1 shows the model prediction of the diametral strain profiles of pressure tubes in Pickering A. Note that the model is fitted to the average strain rate of the Pickering A data at the 3.0 m position, but the shapes of

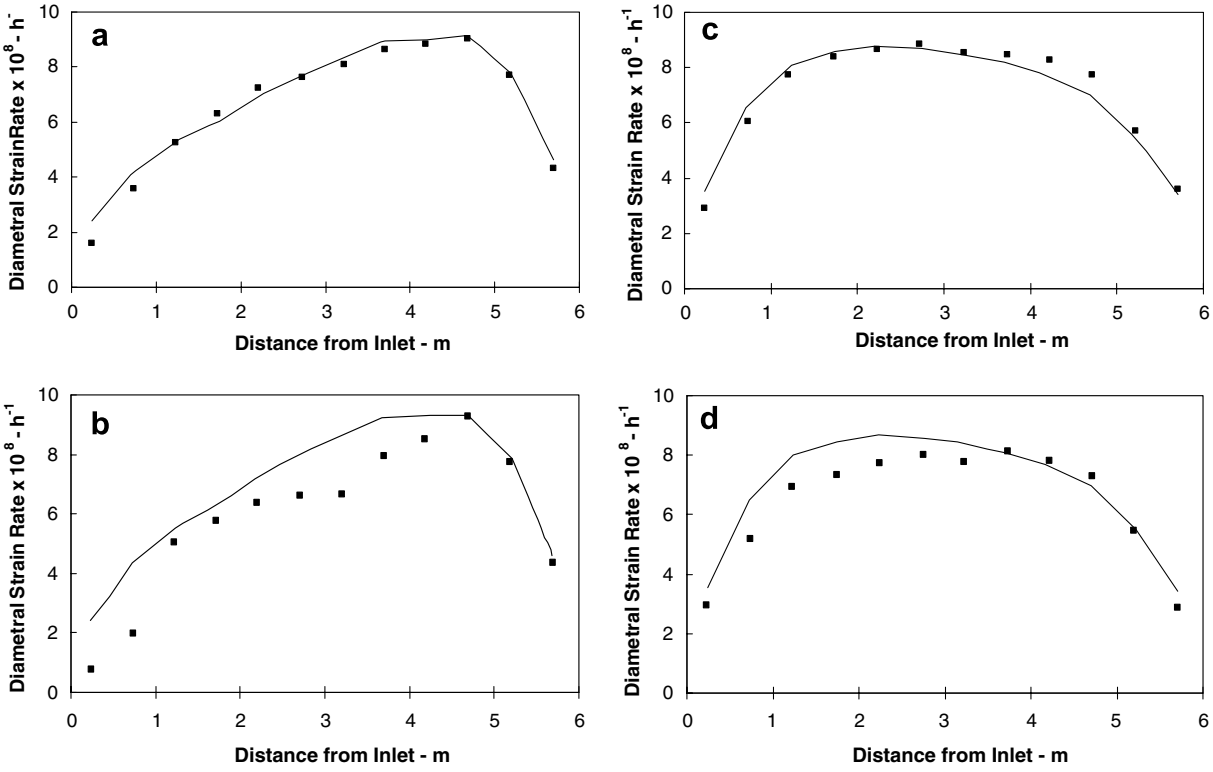

Fig. 11.3.1. Comparison of predicted and measured strain rate profiles for Zr–2.5Nb pressure tubes in a Pickering A reactor: (a,b) back end at outlet and (c,d) back end at inlet, from Ref. [14].

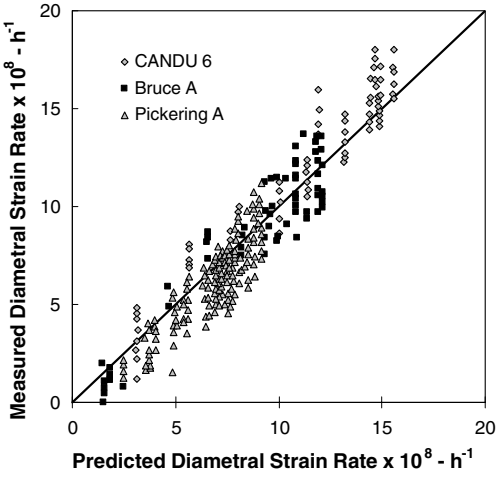

Fig. 11.3.2. Comparison of measured and predicted diametral strain rates of Zr–2.5Nb pressure tube in CANDU reactors, from Ref. [14].

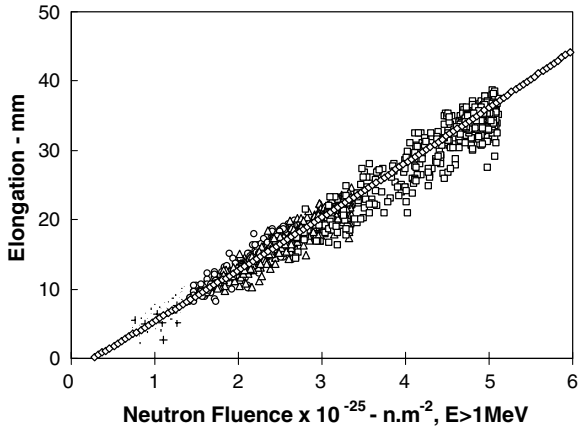

Fig. 11.3.3. Comparison of the model predictions with elongation data for pressure tubes in a Bruce A reactor, from Ref. [14].

the profiles are derived from other information. The model is a reasonably good predictor of the diametral strain rates, Fig. 11.3.2, and elongation rates, Fig. 11.3.3 of Zr–2.5Nb pressure tubes in Bruce A and Pickering A, operating temperatures up to 570 K. It also predicts well the axial and diametral strain rates for small tubes with textures similar to pressure tubes irradiated at high fast neutron flux at 553 and 583 K [12], Fig. 11.3.4, and diametral strain rates for pressure tubes operating at temperatures of up to 670 K at low stress (<80 MPa), Fig. 11.3.5. However, it tends to under-predict peak diametral strain rates for CANDU 6 pressure tubes with outlet temperatures above 570 K, Fig. 11.3.2. This tendency, which at the time was thought to be within the predictive uncertainty of the model, has since proven to be even greater [120].

12. Outstanding issues and future work

Over 40 years of in-reactor testing and over 30 years of operating experience in power reactors have provided a broad understanding of the in-reactor deformation of

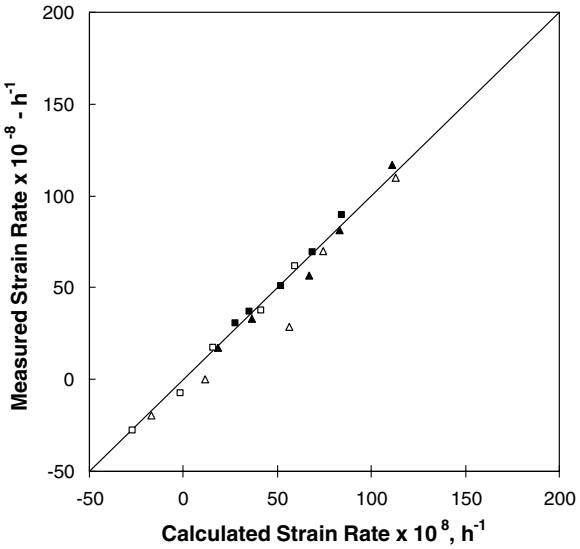

Fig. 11.3.4. Comparison of measured and predicted axial and transverse strain rates for micro-pressure tubes irradiated at $\sim 2 \times 10^{18}$ n m^{-2} s^{-1}, $E > 1$ MeV, in Osiris at 553 and 583 K, from Ref. [75].

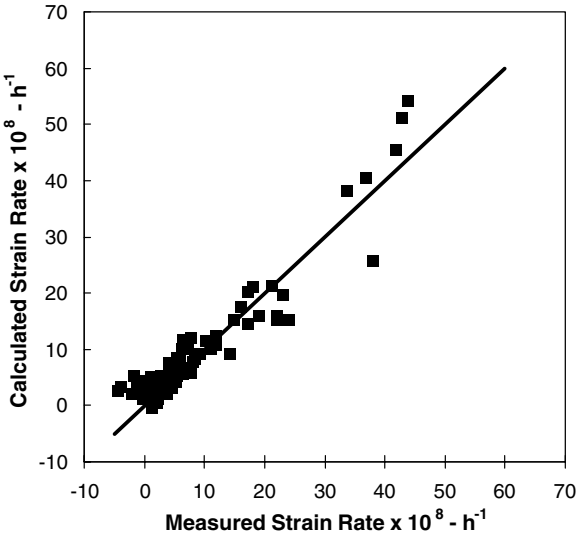

Fig. 11.3.5. Comparison of measured and predicted strain rates of cold-worked Zr–2.5Nb pressure tubes irradiated in the WR1 reactor at temperatures between 573 and 673 K, from Ref. [14].

cold-worked Zr–2.5Nb pressure tubes and an extensive data-base upon which to base models for maintaining existing reactors, and for designing new ones. However there are still significant gaps in our knowledge and on-going work is required in a number of areas.

12.1. Polycrystalline modelling

As stated in Section 11.2, models for anisotropy of creep and growth that are based solely on crystallographic texture suffer from some deficiency when one attempts to extrapolate over a wide range of textures. Other microstructural factors are clearly important. Although the textures of pressure tubes are not likely to change much in the foreseeable future, this deficiency may also indicate a deficiency in the capability for making predictions for stress states for which no experimental information exists. At best, the uncertainties of such predictions are larger than those for predictions for stress states for which experimental data exist. The recent development of accurate techniques to measure the thickness of pressure tubes in-service [121] allows the variation in anisotropy along the length of a pressure tube to be assessed, an important step in verifying or improving the axial variations in deformation represented by Eq. (11.3.7).

12.2. More severe reactor operating conditions

The model described in Section 11.3 was normalized to data from the Pickering A Nuclear Generating Station and tested against data from the Bruce A Station and early data from CANDU 6 units which operate at higher temperatures and fast fluxes than exist in the Pickering A units. Already one could see a tendency to under-predict the CANDU 6 data, Fig. 11.3.2. Although, in 1996, this discrepancy was deemed to be within the predictive error of the model, we now know that there is a systematic under-prediction of peak diametral strain rates for later reactors with more severe operating conditions. This requires at least a rescaling of the parameters of the model, and perhaps a re-examination of the interaction of temperature and fast neutron flux in the range of operating conditions of these reactors.

12.3. Sources of variability

Diametral strain rates of nominally similar pressure tubes, under similar operating conditions in a given power reactor can vary by ±30%, while elongation rates can vary by ±20%. There also appear to be reactor to reactor variations [122]. Some of these variations appear to be due to differences in microstructure, texture and possibly chemical composition, Figs. 4.1–4.5, and are also clearly related in some way to manufacturing variables. This appears to be a profitable area for further study [34]. Similar studies on the variability of mechanical properties of early pressure tubes led to a substantial improvement in fracture toughness by the introduction of quadruple- vs double-arc melting during primary ingot production [123,124].

12.4. Creep at flaws

The principle that creep can relax stresses at flaws has been clearly demonstrated experimentally. The susceptibility of notched specimens of pressure tube material is significantly less if the notched specimen is held at temperature, under load, to allow creep to relax the notch-tip stress prior to testing for DHC susceptibility [125].

The model for localized creep at the high stress regions near flaws is based on a very limited data set and this certainly needs to be augmented.

12.5. Temperature cycling effects

Because they have a high capital cost and a low operating cost, most existing nuclear generating stations operate as base-load electricity suppliers. Future nuclear plants may operate in a load-following mode, particular if, as seems likely, nuclear power occupies a larger share of the electricity supply in some markets. Operating reactors in load-following mode may involve significant temperature changes. The large transients in growth strain observed after temperature changes, see Section 5, suggest that temperature cycling may contribute a component to the strain, different from that predicted by the models presented in Section 11. This area requires further investigation.

12.6. Creep rupture

The case for operating pressure tubes to creep strains of the order of 5% is based on the supposition that pressure tubes will exhibit quasi-superplastic behaviour under irradiation creep conditions because of the low stress sensitivity of the strain rate, see Section 8. As pressure tubes in current reactors are approaching this level of peak diametral strain (some tubes in the older CANDU 6 reactors have strains >4%), it is important to assess the microstructure at the peak-strain location to verify that there is no evidence of impending failure due to an as-yet unidentified mechanism associated with the high levels of radiation-induced mass transport. This is especially important in view of the microchemical changes induced by the thermal flux, see Section 12.7.

12.7. Transmutation effects

A little recognized fact is that Nb transmutes to Mo as a result of irradiation by thermal neutrons. It is estimated that about 25% of the Nb is transmuted to Mo at the mid-core location after 30 years of operation [126]. The alloy content will be changed from 2.5–2.8 wt%Nb to 1.9–2.1 wt%Nb and 0.6–0.7%Mo. There is very little information on irradiation behaviour of alloys containing Mo except for Excel (Zr–3.5 wt%Sn–0.8 wt%Nb–0.8 wt%Mo) which behaves similarly to Zr–2.5Nb, but this information only applies to neutron doses corresponding to only 1–2 dpa, well before any significant long term microstructural evolution begins. Therefore, we have no information on the potential consequences in terms of microstructural or microchemical evolution, and subsequent impact on deformation. Clearly, if such effects are significant they must occur gradually during the first 80% of life, but there still may be some consequences near the end-of-life.

12.8. Creep at the pressure tube ends

The least understood aspect of in-reactor deformation of pressure tubes is the transition region between thermal creep and irradiation creep, i.e., the fast flux range of $0.1–6\times10^{16}$ n m^{-2} s^{-1}, $E>1$ MeV. This corresponds to a region about 0.3 m long, adjacent to the end-fittings at each end of the reactor, where the bending moment is high. The current representation of the creep behaviour in this region is crude, and is not a good match to the data. It is very likely that a more accurate model will change the results of sag and contact predictions, and it is therefore most important that efforts to address the deformation rates in this fast flux range [25] should continue.

Acknowledgements

I would like to acknowledge John Slade of New Brunswick Power for permission to use previously unpublished data from the Point Lepreau Nuclear Generating Station, and Grant Bickel, Pam Simons and Eric Nadeau of AECL for providing the figures showing that data. I would also like to thank Navid Badie, Grant Bickel and Stephen Douglas of AECL for permission to refer to their unpublished data, Malcolm Griffiths of AECL for providing micrographs and Nick Christodoulou of AECL for providing digital versions of some of the figures. The preparation of this review was sponsored by the Natural Sciences and Engineering Research Council of Canada, Ontario Power Generation Inc., the CANDU Owners Group Inc., and Nu-Tech Precision Metals Inc., under the Industrial Research Chair program in Nuclear Materials at Queen's University.

Figs. 2.1.3, 2.1.4, 3.2, 4.1, 4.3–4.5, 5.1.1, 5.1.2, 5.3.1–5.3.4, 5.4.1, 5.6.1, 5.6.2, 6.2.1, 6.6.1, 7.2.1, 9.1–9.6, 11.2.1, 11.3.1–11.3.5 were adapted, with permission, from proceedings of the 6th, 8th, 9th, 10th, 11th, 12th, 13th, 14th and 15th International Symposia on Zirconium in the Nuclear Industry, ASTM STPs 824, 1023, 1132, 1245, 1295, 1354, 1423, 1457 and the Journal of ASTM International Vol. 2 copyright ASTM International, 100 Barr Harbor Drive, West Conshohocken, PA 19428.

Figs. 3.4, 3.5, 5.1.3, 5.5.1, 5.5.2, 6.2.1, 6.3.2, 6.4.1, 6.4.2, 6.4.6, Figs. 8.2, 10.1.1, 10.1.2 and 11.3.4 were adapted with permission from the Journal of Nuclear Materials, Volumes 60, 98, 149, 159, 317 and 335, copyright Elsevier B.V.

References

[1] Canadian Standards Association Standard CSA N286.6 Series 88, Materials Standards for Reactor Components for CANDU Nuclear Power Plants, General Instruction No. 1, 1st Ed., Toronto, 1994.

[2] Canadian Standards Association Standard CSA Z299 Series 85-CAN, Quality Assurance Program – Categories 1, 2, 3 & 4, General Instruction No. 1, 2nd Ed., Toronto, 1997.

[3] Canadian Standards Association Standard CSA N285.2-99-CAN/CSA, Requirements for Class 1C, 2C and 3C Pressure Retaining

Components and Supports in CANDU Nuclear Power Plants, General Instruction No. 1, 2nd Ed., Toronto, 1999.
[4] Canadian Standards Association Standard CSA N289.1-80-CAN3, General Requirements for Seismic Qualification of CANDU Nuclear Power Plants, General Instruction No. 1, 2nd Ed., Toronto, 1992.
[5] Canadian Standards Association Standard CSA N285-4-94-CAN/CSA, Periodic Inspection of CANDU Nuclear Power Plant Components, General Instruction No. 1, 2nd Ed., Toronto, 1994.
[6] Canadian Standards Association Standard CSA N285.8-05, Technical Requirements for In-service Evaluation of Zirconium Alloy Pressure Tubes in CANDU Reactors, Toronto, 2005.
[7] R.A. Holt, H. Wong, Nucl. Energy 41 (2002) 69.
[8] J.R. Hopkins, E.G. Price, R.A. Holt, H.W. Wong, in: ASME/JSME Conference on Pressure Vessels and Piping, San Diego, July 1998.
[9] E.G. Price, R.A. Holt, H.W. Wong, P.J. Ellis, J. Slade, in: Proceedings of the IAEA/COG Technical Meeting on Operating Experience in Heavy Water Reactors, Mangala, Romania, September 1998.
[10] G. Van Drunen, R.J. Dunn, W.R. Mayo, D.A. Scott, Atomic Energy of Canada Ltd., Report AECL-12026, June 1999.
[11] R.R. Hosbons, P.H. Davies, M. Griffiths, S. Sagat, C.E. Coleman, in: Proceedings of the 12th International Symposium on Zirconium in the Nuclear Industry, ASTM STP 1354, 2000, p. 122.
[12] R.A. Holt, A.R. Causey, M. Griffiths, E.T.C. Ho, in: Proceedings of the 12th International Symposium on Zirconium in the Nuclear Industry, ASTM STP 1354, 2000, p. 86.
[13] B.A. Cheadle, C.E. Coleman, D.K. Rodgers, P.H. Davies, C.K. Chow, M. Griffiths, in: Proceedings of the International Conference on CANDU Maintenance, Canadian Nuclear Society, November 1988.
[14] N. Christodoulou, A.R. Causey, R.A. Holt, C.N. Tome, N. Badie, R.J. Klassen, R. Sauve, C.H. Woo, in: Proceedings of the 11th International Symposium on Zirconium in the Nuclear Industry, ASTM STP 1295, 1996, p. 518.
[15] R.A. Holt, A.R. Causey, V. FidlerisProceedings of the International Conference on Dimensional Stability of Irradiated Metals and Alloys, vol. 1, British Nuclear Energy Society, 1983, p. 175.
[16] J. Hopwood, in: Proceedings of the 26th Annual Conference of the Canadian Nuclear Society, paper P23, 2005.
[17] R.A. Holt, N. Christodoulou, A.R. Causey, J. Nucl. Mater. 317 (2003) 256.
[18] N. Badie, R.A. Holt, C.W. Schulte, R.G. Sauve, in: Proceedings of the Ninth Annual Conference of the Canadian Nuclear Society, June 1988.
[19] R.G. Sauve, N. Badie, R.A. Holt, in: Proceedings of the 10th International Conference on Structural Materials in Reactor Technology (SMiRT 10), vol. D, 1989, vol. L, p. 219.
[20] N. Badie, G.D. Morandin, R. Sauve, in: Proceedings of the ASME Pressure Vessel and Piping Conference, Boston, 1999, vol. 385, p. 247.
[21] M. Griffiths, C.K. Chow, C.E. Coleman, R.A. Holt, S. Sagat, V.F. Urbanic, in: Proceedings of the Effects of Radiation on Materials: 16th International Symposium, ASTM STP 1175, 1993, p. 1077.
[22] M. Griffiths, W.G. Davies, G.D. Moan, R.A. Holt, A.R. Causey, S.A. Aldridge, in: Proceedings of the 13th International Symposium on Zirconium in the Nuclear Industry, ASTM STP 1423, 2002, p. 796.
[23] N. Christodoulou, P.A. Turner, B.W. Leitch, C.N. Tomé, N. Badie, R.G. Sauvé, in: Proceedings of the THERMEC 2000, International Conference on Processing and Manufacturing of Advanced Materials, Las Vegas, Nevada, 2000.
[24] B.W. Leitch, N. Christodoulou, C.N. Tomé, P.A. Turner, in: Sixth International Conference on Residual Stress, Oxford, UK, July 2000.
[25] M. Griffiths, N. Christodoulou, S.A. Donohue, in: Proceedings of the 14th International Symposium on Zirconium in the Nuclear Industry, J. ASTM Int. 2 (2005) 686.
[26] J.E. Harbottle, in: C.E. Coleman (Ed.), The Technology of Zirconium, International Atomic Energy Agency, submitted for publication.
[27] D.G. Franklin, G.E. Lucas, A.L. Bement, in: Creep of Zirconium Alloys in Nuclear Reactors, ASTM STP 815, 1983.
[28] B.A. Cheadle, in: Proceedings of the Third International Symposium on Zirconium in the Nuclear Industry, ASTM STP 633, 1977, p. 457.
[29] G.J. Field, J.T. Dunn, B.A. Cheadle, Can. Metall. Quart. 24 (1985) 181.
[30] R.A. Holt, N. Christodoulou, G. Bickel, J. Nucl. Mater., in press.
[31] C.E. Ells, E.F. Ibrahim, A.R. Causey, in: Proceedings of the International Conference on Creep, JSME/IMechE/ASME/ASTM, Tokyo, 1986, p. 59.
[32] L.K.H. Leung, J.S. Jun, G.R. Dimmick, D.E. Bullock, W.W.R. Lynch, H.C. Suk, in: Proceedings of the Seventh International Conference on CANDU Fuel, The Canadian Nuclear Society, Toronto, Ont., 2001.
[33] A.R. Causey, V. Fidleris, S.R. McEwen, C.W. Schulte, in: Proceedings of the 13th International Symposium on Influence of Radiation on Material Properties, ASTM STP 956, 1987, p. 54.
[34] G. Bickel, AECL, unpublished data, 2005.
[35] V. Fidleris, A.R. Causey, R.A. Holt, in: F.A. Garner, D.S. Gelles, F.W. Witten (Eds.), Optimizing Materials for Nuclear Applications, The Metallurgical Society, Inc., Warrendale, PA, 1985, p. 35.
[36] T.P. Byrne, D.R. Metzger, M. Leger, in: Proceedings of the 11th Conference on Structural Mechanics in reactor Technology (SMiRT 11), Tokyo, paper B13/1, 1991.
[37] J.R. Hopkins, in: Proceedings of the Second International Conference on CANDU Maintenance, Canadian Nuclear Society, Toronto, paper 4B, 1987.
[38] M. Liska, B. Churchill, I. Laughlin, in: Proceedings of the Sixth Annual Conference of the Canadian Nuclear Society, CNS, Toronto, 1985, p. 12.9.
[39] R.G. Fleck, E.G. Price, B.A. Cheadle, in: Proceedings of the Sixth International Symposium on Zirconium in the Nuclear Industry, ASTM STP 824, 1984, p. 88.
[40] R. Choubey, S.A. Aldridge, J.R. Theaker, C.D. Cann, C.E. Coleman, in: Proceedings of the 11th International Symposium on Zirconium in the Nuclear Industry, ASTM STP 1295, 1996, p. 657.
[41] M. Griffiths, R.A. Holt, J. Li, S. SaimotoMicrostructural Science, vol. 26, ASM International, Materials Park, 1999, p. 293.
[42] C.E. Coleman, R.W. Gilbert, G.J.C. Carpenter, G.C. Weatherly, in: Phase Stability During Irradiation, The Metallurgical Society of AIME, Pittsburg, 1980, p. 857.
[43] M. Griffiths, J.E. Winegar, Atomic Energy of Canada Ltd., Report AECL-10835, December 1994.
[44] V. Perovic, A. Perovic, G.C. Weatherly, L.M. Brown, G.R. Purdy, R.G. Fleck, R.A. Holt, J. Nucl. Mater. 205 (1993) 251.
[45] R.A. Holt, J. Nucl. Mater. 59 (1976) 234.
[46] R.A. Holt, M. Griffiths, R.W. Gilbert, J. Nucl. Mater. 149 (1987) 51.
[47] M. Griffiths, D. Sage, R.A. Holt, C.N. Tome, Metall. Mater. Trans. 33A (2002) 859.
[48] A. Akhtar, J. Nucl. Mater. 47 (1973) 79.
[49] R.A. Holt, P. Zhao, J. Nucl. Mater. 335 (2004) 520.
[50] J.J. Kearns, U.S. Atomic Energy Commission Research and Development Report (Contract AT-11-1-GEN-14), WAPD-TM-472, Bettis Atomic Power Laboratory, November 1965.
[51] R.A. Holt, E.F. Ibrahim, Acta Metall. 27 (1979) 1319.
[52] R.G. Fleck, J.E. Elder, A.R. Causey, R.A. Holt, in: Proceedings of the 10th International Symposium on Zirconium in the Nuclear Industry, ASTM-STP 1245, 1994, p. 168.
[53] A.R. Causey, AECL, private communication, 2000.
[54] R.A. Holt, J. Nucl. Mater. 159 (1988) 310.
[55] V. Fidleris, J. Nucl. Mater. 159 (1988) 22.
[56] J. Winton, R.A. Murgatroyd, in: J.P. Pemsler, E.C.W. Perryman, W.W. Smelzer (Eds.), Zirconium and its Alloys, The Electrochemical Society, Inc., New York, 1966, p. 322.

[57] J.D. Parker, V. Perovic, M. Leger, R.G. Fleck, in: Proceedings of the Ninth International Symposium on Zirconium in the Nuclear Industry, ASTM STP 939, 1987, p. 86.
[58] R.A. Holt, R.G. Fleck, in: Proceedings of the Eighth International Symposium on Zirconium in the Nuclear Industry, ASTM STP 1023, 1989, p. 705.
[59] R.A. Holt, A.R. Causey, J. Nucl. Mater. (2004) 529.
[60] T.S. Gendron, R.A. Holt, R.G. Fleck, in: Proceedings of the International Conference on Irradiation Technology, Commissariat a l'Energie Atomique and Commmission of the European Communities, Paris, paper V4, 1992.
[61] R.A. Holt, R.G. Fleck, in: Proceedings of the Ninth International Symposium on Zirconium in the Nuclear Industry, ASTM STP 1132, 1991, p. 218.
[62] R.G. Fleck, R.A. Holt, V. Perovic, J. Tadros, J. Nucl. Mater. 159 (1988) 75.
[63] G.M. Hood, H. Zou, D. Gupta, J. Schultz, J. Nucl. Mater. 223 (1995) 122.
[64] A.D. King, G.M. Hood, R.A. Holt, J. Nucl. Mater. 185 (1991) 174.
[65] S.N. Buckley, in: D.J. Littler (Ed.), Properties of Reactor Materials and Effects of Radiation Damage, Butterworth, London, 1962, p. 413.
[66] C.N. Tomé, N. Christodoulou, Philos. Mag. A 80 (2000) 1407.
[67] R.A. Holt, J. Nucl. Mater. 82 (1979) 419.
[68] R.A. Holt, A.R. Causey, J. Nucl. Mater. 150 (1997) 306.
[69] R.A. Holt, T.M. Holden, A.R. Causey, V. Fidleris, in: Proceedings of the 10th Risø International Symposium on Metallurgy and Materials Science: Materials Architecture, Risø National Laboratory, Roskilde, Denmark, 1989, p. 383.
[70] C.N. Tomé, N. Christodoulou, P.A. Turner, M.A. Miller, C.H. Woo, J. Root, T.M. Holden, J. Nucl. Mater. 227 (1996) 237.
[71] A.R. Causey, C.H. Woo, R.A. Holt, J. Nucl. Mater. (1988) 225.
[72] O.J.V. Chapman, R.J. McElroy, B.E. Sheldon, in: Proceedings of the Sixth International Symposium on Zirconium in the Nuclear Industry, ASTM STP 824, 1984, p. 343.
[73] N. Christodoulou, P.A. Turner, C.N. Tome, C.K. Chow, R.J. Klassen, Metall. Mater. Trans. A 33A (April) (2002) 1103.
[74] E.F. Ibrahim, R.A. Holt, J. Nucl. Mater. 91 (1980) 311.
[75] A.R. Causey, R.A. Holt, N. Christodoulou, E.T.C. Ho, in: Proceedings of the 12th International Symposium on Zirconium in the Nuclear Industry, ASTM STP 1354, 2000, p. 74.
[76] P.A. Ross-Ross, V. Fidleris, D.E. Fraser, Can. Metall. Quart. 11 (1972) 101.
[77] D.E. Fraser, P.A. Ross-Ross, A.R. Causey, J. Nucl. Mater. 46 (1973) 281.
[78] A.R. Causey, J. Nucl. Mater. 98 (1981) 313.
[79] C.E. Coleman, A.R. Causey, V. Fidleris, J. Nucl. Mater. 60 (1976) 185.
[80] R.J. Klassen, V. Fidleris, AECL unpublished data, 1996.
[81] J. Schroeder, M. Holicky, J. Nucl. Mater. 33 (1969) 52.
[82] B.A. Cheadle, S.A. Aldridge, J. Nucl. Mater. 47 (1973) 255.
[83] A.R. Causey, R.A. Holt, S.R. MacEwen, in: Proceedings of the Eighth International Symposium on Zirconium in the Nuclear Industry, ASTM-STP 824, 1984, p. 269.
[84] C.E. Coleman, J.F.R. Amber, Rev. Coat. Corros. 3 (1979) 105.
[85] M. Resta-Levi, M.P. Puls, in: Proceedings of the 18th International Conference on structural Mechanics in reactor Technology (SMiRT 18), Beijing, paper G10-3, 2005.
[86] M.F. Banham, A.J. Fudge, J.A. Tibbles, B.E. Sheldon, R.G. Fleck, R.A. Holt, in: Proceedings of the Seventh ASTM Euratom Symposium on Reactor Dosimetry, Kluwer Academic Publishers, Norwell, MA, 1990, p. 749.
[87] D.A. Woodford, Mater. Sci. Eng. 4 (1969) 146.
[88] D.A. Woodford, Trans. Am. Soc. Met. 62 (1969) 291.
[89] E.F. Ibrahim, J. Nucl. Mater. 96 (1981) 297.
[90] K.P. Steward, B.A. Cheadle, Trans. AIME 239 (1967) 504.
[91] M. Griffiths, J.F. Mecke, J.E. Winegar, in: Proceedings of the 11th International Symposium on Zirconium in the Nuclear Industry, ASTM-STP 1295, 1996, p. 580.
[92] V.F. Urbanic, M. Grifiths, in: Proceedings of the 12th International Symposium on Zirconium in the Nuclear Industry, ASTM-STP 1354, 2000, p. 641.
[93] M. Griffiths, P.H. Davies, W.G. Davies, S. Sagat, in: Proceedings of the 13th International Symposium on Zirconium in the Nuclear Industry, ASTM-STP 1423, 2002, p. 507.
[94] R. Bullough, M.H. Wood, J. Nucl. Mater. 90 (1980) 1.
[95] R.A. Holt, C.H. Woo, C.K. Chow, J. Nucl. Mater. 205 (1993) 293.
[96] C.H. Woo, Radiat. Eff. Defects Solids 144 (1998) 145.
[97] C.H. Woo, U.M. Gösele, J. Nucl. Mater. 119 (1983) 219.
[98] C.H. Woo, J. Nucl. Mater. 159 (1988) 237.
[99] H. Weidersich, Radiat. Eff. 12 (1972) 111.
[100] J.R. Matthews, M.W. Finnis, J. Nucl. Mater. 159 (1988) 257.
[101] A.H. Cottrel, Atomic Energy Research Establishment – Harwell report AERE M/M1 02, 1955.
[102] P.K. Madden, R. Hesketh, Central Electricity Generating Board Report, CEGB – RD/B/N3113, 1975.
[103] G.R. Piercy, J. Nucl. Mater. 26 (1968) 18.
[104] J. Weertman, Trans. Am. Soc. Met. 61 (1968) 681.
[105] S.R. MacEwen, V. Fidleris, Philos. Mag. 31 (1975) 1149.
[106] J. Gittis, Philos. Mag. 25 (1972) 345.
[107] A.A. Semenov, C.H. Woo, J. Nucl. Mater. 233–237 (1996) 1045.
[108] P.T. Heald, M.V. Speight, Acta Metall. 23 (1975) 1389.
[109] R. Bullough, M.R. Haynes, J. Nucl. Mater. 65 (1977) 184.
[110] W.G. Wolfer, J. Nucl. Mater. 90 (1980) 175.
[111] R. Hill, The Mathematical Theory of Plasticity, Oxford University, London, 1954.
[112] A.R. Causey, J. Nucl. Mater. 54 (1974) 64.
[113] M.J. Pettigrew, S.B. Lambert, in: Proceedings of the Fifth International Conference of Structural Mechanics in Reactor Technology (SMiRT-5), Berlin, paper L8-2, 1979.
[114] R.G. Sauvé, in: Proceedings of the 13th Annual Reactor Simulation Symposium, Atomic Energy of Canada Ltd., Report CRNL-4139, 1987.
[115] C.N. Tomé, C.B. So, C.H. Woo, Philos. Mag. A67 (1993) 917.
[116] C.N. Tomé, N. Christodoulou, R.A. Holt, C.H. Woo, R.A. Lebensohn, P.A. Turner, in: Proceedings of the 15th Risø International Symposium on Materials ScienceNumerical Predictions of deformation Processes and the Behaviour of Real Materials, Risø National Laboratory, Roskilde, Denmark, 1994.
[117] N. Christodoulou, A.R. Causey, C.H. Woo, C.N. Tomé, R.J. Klassen, R.A. Holt, in: 16th International Symposium on the Effects of Radiation on Materials, ASTM STP 1175, 1993, p. 1111.
[118] A.R. Causey, J.E. Elder, R.A. Holt, R.G. Fleck, in: Proceedings of the 10th International Symposium on Zirconium in the Nuclear Industry, ASTM-STP 1245, 1994, p. 202.
[119] P.A. Turner, C.N. Tomé, N. Christodoulou, C.H. woo, Philos. Mag. A 79 (1999) 2505.
[120] R.A. Holt, A.R. Causey, W.G. Davies, unpublished data, 1998.
[121] W.R. Mayo, G. Van Drunen, D. Kalenchuk, R. Gunn, in: Proceedings of the Sixth CNS International Conference on CANDU Maintenance, Canadian Nuclear Society, Toronto, Ont., paper 3a20, 2003.
[122] N. Badie, D. Leemans, private communication, 2003.
[123] I. Aitchison, P.H. Davies, J. Nucl. Mater. 203 (1993) 206.
[124] J.R. Theaker, R. Choubey, G.D. Moan, S.A. Aldridge, L. Davis, R.A. Graham, C.E. Coleman, in: Proceedings of the 10th International Symposium on Zirconium in the Nuclear Industry, ASTM-STP 1245, 1994, p. 221.
[125] S. Sagat, G.W. Newman, D.A. Scarth, in: Proceedings of the International Conference for Hydrogen Effects on Material Behaviour and Corrosion Deformation Interactions, Moran, Wyoming, 2002.
[126] S. Douglas, AECL, unpublished data, 2005.